

NASA  
Technical  
Paper  
3225

ARL  
Technical  
Report  
30

February 1993

IN-39  
151052  
P.59

# Experimental and Analytical Investigation of Dynamic Characteristics of Extension-Twist-Coupled Composite Tubular Spars

Renee C. Lake,  
Amir P. Izadpanah,  
and Robert M. Baucom

(NASA-TP-3225) EXPERIMENTAL AND ANALYTICAL INVESTIGATION OF DYNAMIC CHARACTERISTICS OF EXTENSION-TWIST-COUPLED COMPOSITE TUBULAR SPARS (NASA) 59 p

N93-20585

Unclassified

H1/39 0151052



ORIGINAL CONTAINS  
COLOR ILLUSTRATIONS

491658

NASA  
Technical  
Paper  
3225

ARL  
Technical  
Report  
30

1993

Experimental and Analytical  
Investigation of Dynamic  
Characteristics of  
Extension-Twist-Coupled  
Composite Tubular Spars

Renee C. Lake  
*Vehicle Structures Directorate*  
*U.S. Army Research Laboratory*  
*Langley Research Center*  
*Hampton, Virginia*

Amir P. Izadpanah  
*Sterling Software*  
*Federal Systems Group*  
*Palo Alto, California*

Robert M. Baucom  
*Langley Research Center*  
*Hampton, Virginia*



National Aeronautics and  
Space Administration  
Office of Management  
Scientific and Technical  
Information Program

The use of trademarks or names of manufacturers in this report is for accurate reporting and does not constitute an official endorsement, either expressed or implied, of such products or manufacturers by the National Aeronautics and Space Administration or the United States Army.

## Summary

The results from an in-house study aimed at improving the dynamic and aerodynamic characteristics of composite rotor blades through the use of extension-twist elastic coupling are presented. A set of extension-twist-coupled composite tubular spars, representative of the primary load-carrying structure within a helicopter rotor blade, was manufactured with four plies of T-650/42 graphite fiber with ERLX 1925-2 epoxy resin in a plain weave cloth prepreg. The  $0^\circ$ - $90^\circ$  cloth weave was rotated off-axis to achieve a  $[+20^\circ]_4$  laminate. These spars were noncircular in cross-section design and were therefore subject to warping deformations. Three different cross-sectional geometries were developed: D-shape, square, and flattened ellipse. Three spars of each type were fabricated in order to assess the degree of repeatability in the manufacturing process of extension-twist-coupled structures. Results from free-free vibration tests of the spars were compared with results from normal modes and frequency analyses of companion shell-finite-element models developed in MSC/NASTRAN. Five global or nonshell modes were identified within the frequency bandwidth from 0 to 2000 Hz for each spar. Because of some anomalies encountered in the testing and subsequent determination of the modal properties for two of the three D-shape spars, the results for only one D-shape spar were determined. The frequencies and associated mode shapes were correlated with analytical results, and the agreement was within 13.8 percent. Frequencies corresponding to the five global mode shapes for the three square spars agreed within 9.5, 11.6, and 8.5 percent of their analytical counterparts. Five global modes were similarly identified for the three elliptical spars and agreed within 4.9, 7.7, and 9.6 percent of the analytical results.

## Introduction

The design of advanced rotor blades is becoming significantly influenced with the incorporation of composite materials technology. Such designs offer considerable advantages with respect to strength and weight criteria, in addition to providing a means of efficiently controlling static and dynamic response through the implementation of elastic tailoring. The ability to analytically predict the dynamic characteristics of composite rotor blades exhibiting elastic coupling is essential to the implementation of elastic coupling in these applications. However, as a result of advancements in elastically tailored structural design, a corresponding increase in the level of analytical complexity is introduced. This complex-

ity is particularly true of the dynamic behavior, as the elastic couplings can have a substantial influence on the vibration characteristics. The identification of the vibration characteristics (i.e., natural frequencies and mode shapes) of a rotor blade is necessary for the prediction of its resonant behavior and is essential in aeroelastic stability analyses. Therefore, it is necessary to determine the accuracy of existing analyses applicable to elastically coupled composite rotor blades. The validation of these analyses is further dependent upon the establishment of an extensive experimental data base for the dynamic characteristics of elastically coupled structures, which has yet to be developed.

Many examples of recent analytical treatments of composite rotor blade structures exist in the literature and include advanced beam and plate finite-element formulations. The inclusion of so-called nonclassical effects, which include transverse shear, warping, and geometric nonlinearities, has been emphasized in these formulations and attempts to account for the complex structural behavior of advanced helicopter rotor blades. For example, in reference 1, the warping effects of composite beams undergoing large deflections and large rotations in rotating and nonrotating conditions were established. Verification of this analysis was performed by comparing numerical results with those obtained experimentally in reference 2, producing excellent correlation for flapping and lead-lag frequencies. The dynamic behavior of elastically coupled composite blades subject to large deflections was also studied in reference 3. Several types of elastically coupled graphite-epoxy spars, including bending-twist-coupled and extension-twist-coupled designs for three varying thicknesses, were fabricated in addition to uncoupled designs to investigate the influence of elastic couplings in laminate designs. The influence of static deflections due to a natural gravity load on the small amplitude vibrations was also studied for each spar. Results from the experimental-analytical investigation showed that the presence of static deflections has a significant influence on torsional and lead-lag modes and frequencies. This study was further expanded in reference 4 to investigate the effects of large amplitude vibrations, and similar findings resulted.

The influence of ply lay-ups on the natural frequencies and mode shapes of composite beams was addressed in reference 5 where a mixed finite-element method was used. Numerical results showing the variation in frequency versus ply angle were presented for a thin-walled tube with circular cross section for a variety of laminate designs, including

an extension-twist-coupled laminate, where several variational characteristics were observed. Specifically, some extension-twist-coupled modes occurred in pairs, with one mode having extension and torsion components of opposite signs, whereas the components of the companion mode shared the same sign. The characteristic shape of the coupled modes, as well as the sequential order of frequencies, was found to vary with ply angle. In addition, analytical results for a laminated solid rectangular cross section were compared with experimental results from reference 6 for ply lay-ups of  $0^\circ$ ,  $15^\circ$ ,  $30^\circ$ , and  $90^\circ$ . Good correlation was obtained, although only experimental frequencies associated with the coupled vertical bending/torsion modes were available.

The dynamic behavior of an extension-twist-coupled composite circular tube was analytically and experimentally studied in reference 7. An equivalent-beam finite-element model based on the coupled-beam analysis developed in reference 8 was used in conjunction with a detailed MSC/NASTRAN finite-element model to predict the natural frequencies and mode shapes. Experimental data from a free-free vibration test of a thin-walled composite test spar were used to validate the finite-element models. Results from this study demonstrated that natural frequencies and mode shapes could be obtained within practical engineering accuracy for nonwarping-prone extension-twist-coupled composite structures. However, the equivalent-beam finite-element model did not accurately predict the frequencies for mode shapes influenced by elastic coupling.

The global response characteristics of general thin-walled anisotropic beams which exhibit shear and warping deformations were studied in reference 9. Results from an anisotropic beam finite-element analysis were experimentally verified with a set of static axial tests performed on different configurations of extension-twist-coupled tubular beam structures to assess the influence of warping-prone cross-sectional geometries. Test results demonstrated that bending-related warping effects have significant influence on beam-like structures and are amplified by the extension-twist coupling, whereas the effects of torsion-related warping were not found to be significant for practical rotor structures. This investigation, however, only addressed the static behavior of extension-twist-coupled composite spar designs and leaves the question of how such designs influence the dynamic characteristics.

An in-house research program aimed at improving the dynamic and aerodynamic characteristics of composite rotor blades through the use of elastic couplings has been initiated to address

this need. Extension-twist elastic coupling, which exhibits coupling among the extensional and torsional stiffnesses of a structure, was chosen for this study because of its potentially advantageous application to tilt rotor blades. The objectives of this program were to provide a basis for understanding the mechanics of elastic coupling as applied to rotor blade structures and also to develop verifiable finite-element modeling methodologies that are capable of accurately representing this phenomenon. A series of analytical and experimental studies has been designed to demonstrate the potential improvements to tilt rotor blade performance. Analytical models would be validated through the static and dynamic testing of a series of elastically coupled composite test spars representative of rotor blade spars. These test spars include untwisted, thin-walled tubes of circular cross section and progress to more advanced designs involving noncircular cross sections and pretwist. Such designs introduce additional complexity as they are subject to out-of-plane warping deformations. This will lead to the development of low twist, model-scale composite rotor blades, with subsequent whirl and wind-tunnel tests designed to demonstrate the feasibility of changing blade twist as a function of rotor speed. The analytical-experimental study of these blades will provide the basis for the design and development of a highly twisted composite tilt rotor blade design incorporating extension-twist elastic coupling.

This paper presents recent results from an in-house investigation of the dynamic characteristics of thin-walled extension-twist-coupled composite tubular spars. Results from a normal modes analysis of shell-finite-element models were compared with experimental results obtained from free-free vibration tests of extension-twist-coupled composite tubular spars. These spars were noncircular in cross-section design and were therefore subject to warping deformations. Because the presence of extension-twist coupling in a laminate acts to "magnify" the warping effect, a significant influence on the dynamic behavior may result. Such warping-prone designs are more closely representative of true rotor blade spar structures and require thorough investigation of the dynamic characteristics.

## Symbols

$E_{11}$	extension modulus (spanwise), lb/in <sup>2</sup>
$E_{22}$	extension modulus (chordwise), lb/in <sup>2</sup>
FEA	finite-element analysis
$G_{12}$	shear modulus, lb/in <sup>2</sup>

<i>j</i>	response degree of freedom
MAC	modal assurance criteria
MCF	modal confidence factor
MMIF	multivariate mode indicator function
<i>m</i>	number of response degrees of freedom
<i>t<sub>ply</sub></i>	lamina thickness, in.
<i>v<sub>12</sub></i>	Poisson ratio
<i>ρ</i>	density, lb/in <sup>3</sup>
<i>ψ<sub>1</sub></i>	<i>m</i> -dimensional vector representing normalized mode shape 1
<i>ψ<sub>2</sub></i>	<i>m</i> -dimensional vector representing normalized mode shape 2
Superscript:	
*	complex conjugate

## Test Models

### Composite Test Spars

Nine composite tubular spars were fabricated for dynamic testing. Each tube was 24 in. in length and was fabricated with four plies of T-650/42 graphite fiber with ERLX 1925-2 epoxy resin in a plain weave cloth prepreg. This material system is manufactured by Amoco Performance Products, Inc. The associated material properties, obtained from coupon tests conducted in reference 9, are shown in table 1. The 0°–90° cloth weave was rotated off-axis to achieve a [+20°]4 ply stacking sequence. This symmetric arrangement of ply angles provides a mechanism for extension-twist coupling in a thin-walled cellular structure through the interaction of extensional and torsional deformations. Specifically, the laminate shears in response to an axial load and causes the cell structure to develop a net twist deformation. In addition, a secondary type of coupling that was inherent in this type of extension-twist-coupled design acted to couple the bending and shear deformations. This parasitic bending-shear coupling influences a structure such that a shear deformation in a given geometry plane results from a bending deformation in an orthogonal plane.

Three different cross-sectional geometries were manufactured: D-shape, square, and flattened ellipse. In order to assess the degree of repeatability in the manufacturing process of extension-twist-coupled structures, three spars of each type cross section were fabricated. These spars were given a three letter designation Vci, where V denotes vibration test article, c refers to cross section (i.e., D-shape, Square,

Elliptical), and i refers to spar number (i.e., 1, 2, 3). Figure 1 depicts the three cross-sectional shapes with the associated dimensions. Although all spars were designed to have a nominal wall thickness of 0.030 in., the actual wall thicknesses varied slightly because of the manufacturing process. Because an exact spanwise variation of the wall thickness was difficult to accurately measure by nondestructive means, an average wall thickness was computed for each spar by dividing the weight of the spar by the product of the associated material density, spanwise length, and contour length. This average thickness was used in the finite-element analysis models of the spars. A summary of the average wall thicknesses determined in this manner as well as the percent difference from the design value appears in table 2 along with the measured weight for each spar. The deviation in wall thickness was generally quite small (within 2.3 percent of the design value), except for the elliptical spars. Average deviations of approximately 10 percent were observed in this subset of spars. Potential causes for the marked differences in the elliptical spar wall thicknesses may have precipitated from a change in fabrication personnel during this part of the manufacturing phase. Factors such as the temperature rise rate during the cure cycle and wrapping of the prepreg during the lay-up procedure are integral in the fabrication process and inconsistencies in either or both of these variables could have conceivably contributed to the differences noted.

### Spar Fabrication Process

The thin-walled tubular spars were fabricated by utilizing an expandable rubber mandrel and a segmented aluminum female mold configured to the desired external spar geometry. The rubber mandrel was sized to accommodate the composite wall thickness and a free lateral expansion gap of approximately 0.020 in. prior to contact with the surface of the female mold during processing. A (mild) steel rod was placed in the center of the mandrel to provide stiffness for handling purposes after consolidation of the room temperature vulcanizing silicon rubber. After the rubber was cast, cured, and removed from the sizing tool, it was sprayed with a wet coat of fluorocarbon release agent and dried in an air circulating oven. The mandrel was then ready for application of the graphite-epoxy cloth composite.

Figure 2 shows the silicon rubber mandrel and the initial wrap of composite material which has been cut to the desired fiber orientation. The wrapping procedure began by aligning the rubber tool with one edge of the precut composite material as shown in figure 3. Subsequent layers of composite material

were applied to the assembly by continuing to wrap successive layers of composite in the proper fiber orientation, as shown in figure 4. Once the desired thickness was built up onto the rubber mandrel, the assembly was placed in the female aluminum tool cavity (fig. 5) and the cover plate was secured by bolts. A control thermocouple was inserted into the material at one end and the tool was placed in an air circulating oven. The temperature of the oven was increased at a rate of approximately 10°F/min until the spar reached the cure temperature of 350°F. Upon heating, the rubber mandrel expanded, which forced the composite material against the surface of the female mold. The rubber maintained a pressure of approximately 200 psi on the composite laminate at 350°F. This condition was held for 1 hour for complete composite cure. The assembly was cooled, removed from the oven, and disassembled. The rubber core shrank during the cooling process, which allowed free removal from the composite tube spar. Examples of the cured composite tube spars are shown in figure 6.

Richard Bennett, Materials Processing and Fabrication Division, participated in the manufacturing of the elliptical spars.

## Test Results

### Vibration Test Setup

The vibration test setup used to determine the dynamic characteristics of the composite tubes is shown in figure 7. The test spars were suspended from a support structure with light rubber tubing to simulate a free-free boundary condition. A calibrated impact hammer provided the input excitation for the spar. The test procedure consisted of a roving hammer concept such that impacts at multiple locations along the structure were made while acquiring response data from a fixed location. A three-axis accelerometer transducer configuration was mounted on one end of each spar. (See fig. 8.) The configuration incorporated three single-axis piezoelectric accelerometers, which were affixed to an aluminum mounting block to form a triaxial accelerometer arrangement. This served as the reference point for subsequent measurements. Smaller blocks were used on the elliptical and D-shape spars to facilitate vertical and lateral impacts on the flat and curved surfaces. A list of the block types and their corresponding weights is given in table 3.

A prescribed set of excitation points was chosen to coincide, as closely as possible, with the corresponding grid points of the finite-element model which was formed for each spar. By doing this, an accurate

representation of grid point deformations could be obtained when comparing test and analysis models. The excitation and response point degrees of freedom (location and direction) for each spar are listed numerically in tables 4 through 10 and are illustrated for each spar type in figure 9. Twelve locations were excited in both the lateral ( $Y$ ) and vertical ( $Z$ ) directions for each square spar by using a configuration of two parallel rows of six axial locations. A similar arrangement was employed for the D-shape and elliptical spars, although vertical ( $Z$ ) inputs were omitted along the leading edge of the D-shape spar (grid points 7–12), as well as the lateral ( $Y$ ) inputs along the top of the elliptical spars (grid points 1–6). In the latter case, significant difficulty was encountered when attempting lateral impacts on the upper (flat) surface of the ellipse because of the low shearing modulus of the cyanoacrylate adhesive used to mount the aluminum blocks. Therefore, only impacts which were perpendicular to the shearing plane of the adhesive were obtained at these locations. Additionally, a slight shift in excitation point location from the desired location was necessary in a few instances to achieve a cleaner frequency input spectrum for a spar. This caused a slight nonuniformity in excitation point locations. This shift was usually required whenever slight anomalies in the composite skin were encountered (i.e., excessive accumulation or depletion of resin, inconsistent fabric weave).

### Data Acquisition System

The vibration test of the spars was performed with the Hewlett-Packard 3565S modal testing/data acquisition system. (See fig. 10.) This system is self-contained with respect to hardware components and consists of a front end (i.e., input and source modules, charge amplifiers, signal processing modules), central processing unit (cpu), fixed disk drives, an optical disk drive, and a magnetic tape drive. The front end is capable of simultaneously acquiring up to 8 channels of data with a frequency range of 50 kHz.

Modal data acquisition was performed by the front end, under the control of the Hewlett-Packard Virtual Instrument for Test and Analysis (HP-VISTA) signal processing software (ref. 10). The VISTA software was used to collect data from the measurement hardware and served as a tool for analysis of measurement results. It effectively transformed the workstation into an “analyzer,” or virtual instrument. The raw analog signals generated by the accelerometers or force transducers were fed into the front end and passed through analog-to-digital filters and antialiasing filters. The resulting digital signals

were then processed by the fast Fourier transform (FFT) algorithm and transformed into the frequency domain. The transfer functions were stored as binary files on disk for subsequent processing and analysis and/or displayed on the monitor for viewing.

Test data were obtained for each spar over the frequency bandwidth from 0 to 3200 Hz. The block size, which determined the number of digitized samples within the time record, was 4096 (real), with a frequency resolution of 2.0 Hz. The associated time length of actual data acquisition was 500 msec/data average. A total of 30 data averages was obtained at each excitation point location for all spars.

The associated data files were then ported to the modal analysis software, I-DEAS Tdas (test data analysis software), which is a general purpose test data analysis package developed by Structural Dynamics Research Corporation (ref. 11). The porting of these data was facilitated by a Hewlett-Packard Modal Data Manager, a utility software program (ref. 12), which assembled the individual frequency response function files created by VISTA to produce a formatted file in which a matrix of frequency response functions was stored. This file format was the means by which data were transferred to I-DEAS Tdas, which extracted modal parameters (frequency, mode shape, and damping information) from the transfer functions.

### Data Reduction Techniques

The data reduction phase of this study is perhaps most easily explained in terms of five procedure steps involving curve-fitting techniques, estimating curve-fit parameters, determining residues, calculating mode shapes, and correlation.

**Step 1—curve-fitting techniques.** The Tdas software provided several curve-fitting techniques for the extraction of frequency, amplitude, damping, and phase information for a given mode. These techniques included single-degree-of-freedom curve fits, such as circle fit and peak or valley searches, as well as multiple-degree-of-freedom curve fits, which included complex exponential, direct parameter, and polyreference techniques. The polyreference curve-fitting technique (ref. 13) was chosen to extract the modal parameters for the test spars. This time domain curve-fitting technique uses the impulse response function (inverse of the Fourier transform of the frequency response function) from single or multiple excitation/reference locations in a global least-squares manner. This technique is advantageous because all the available frequency response functions may be used to calculate a global estimate for frequency, damping, and residue; thereby

a more complete description of the modal system is provided. The damped natural frequencies and corresponding damping ratios are first extracted from the acquired time data, followed by calculation of the residues (amplitude and phase). The polyreference technique is useful for multiple-input/multiple-output (MIMO) applications and situations where closely coupled or coincident modes exist. The curve-fitting procedure for the polyreference technique is an iterative process, involving the construction of a correlation matrix which identifies the reference coordinates to be used (i.e., grid point number and direction), the analysis bandwidth, and the maximum number of roots allowed in the estimation. The accuracy of the polyreference technique is dependent upon user-specified estimates of the number of roots present in the frequency range of interest.

### *Step 2—estimating curve-fit parameters.*

An analytical tool designed to aid the user in the determination of the root estimate, known as the multivariate mode indicator function (MMIF), was used in this study. The MMIF can detect the presence of modes within the frequency range of interest, as well as repeated roots, by using the frequency response functions from a given set of reference (response) locations. Conceptually, the MMIF can be thought of as a graphical representation of the ratio of the kinetic energy of in-phase responses to the kinetic energy of the total response plotted as a function of frequency. This ratio is minimized so that the real part of the response is forced to be as small as possible compared with the total response. Minima observed in this plot indicate real normal modes that can be excited within the structure for a given set of reference locations. The number of mode indicator functions in the MMIF is equal to the number of reference coordinates chosen, up to a maximum of three. Three reference coordinates,  $1X_+$ ,  $1Y_-$ ,  $1Z_+$  (grid point 1 in the positive  $X$ , negative  $Y$ , and positive  $Z$  directions, respectively), were selected in this study; therefore, three functions (primary, secondary, and tertiary) were calculated. The MMIF can detect repeated roots which may exist in the structure via coincident minima in the secondary and tertiary functions. A more detailed derivation and explanation of the MMIF can be found in reference 14.

Once the MMIF has been calculated, the number of minima as well as the corresponding natural frequencies can be determined. This determination, which can be performed by visual inspection or through a curve-fit procedure, establishes an initial estimate for the number of roots within the frequency range for the polyreference curve-fit method. The

estimate of roots is an iterative process and judgment is required by the analyst because computational roots (roots which have no physical significance) are also produced by the curve fit and must be identified and eliminated.

**Step 3—determining residues.** Once the frequency and damping terms have been estimated, real or complex residues (amplitude and phase) are calculated based on the specified references and responses. Residues of the real type imply that the phase angles of the associated mode shape differ by 0° or 180° such that all the structural points physically reach their maximum displacements at the same time. Real-type modes are based on proportional damping. A mode shape of complex type exhibits nonproportional damping, where the phase angles can have values other than 0° or 180°, and therefore physically reach their maximum displacements at different times. In instances where damping is light, such as that anticipated in this investigation, the assumption of real-type modes is generally valid.

A feature within the polyreference algorithm known as the modal confidence factor or MCF (ref. 15) was used as an aid to discriminate between computational and physical modes. The MCF takes advantage of the redundant phase relationships that are satisfied by physical modes but not by computational modes and, therefore, represents a measure of how well a given mode conforms to this relationship. The MCF assumes a value near unity for physical modes and a value less than unity (typically less than 0.8) for computational modes. The theory behind the MCF is derived in reference 15.

**Step 4—calculating mode shapes.** Mode shapes corresponding to the real roots identified in the previous step were generated and scaled to a user-specified response coordinate, usually a driving point measurement. The mode shapes for all spars were scaled to their respective 1Z\_ driving point response, which is defined as the measurement made at the same degree of freedom as that of the excitation (i.e., grid point 1 in the negative Z direction). The resultant mode shapes were displayed and animated with simplified graphics models representative of each of the test spars. These models consisted of grid points which geographically corresponded to the excitation points on the spar and were connected by plate elements as a means of defining the spar outline. Because data were obtained at only two lateral locations for each spar (fig. 9), the graphics models appeared planar (two-dimensional).

**Step 5—correlation.** Once the modal properties of the structures were determined, a comparison

of the test and analysis mode shapes was performed with the modal assurance criteria (MAC) matrix. The MAC matrix, which is a three-dimensional matrix, is useful for identifying mode shapes that are similar to each other and can be calculated for test versus test, analysis versus analysis, or test versus analysis mode shapes. The matrix is constructed such that the rows and columns of the matrix correspond to test and/or analysis mode shapes, and the vertical axis corresponds to the associated MAC value. The MAC value is a scalar ranging from zero to unity and represents the linear dependence or similarity of a pair of mode shapes, with unity indicating perfect similarity and zero indicating total dissimilarity. Although this value may be regarded as a measure of orthogonality, it does not constitute a true orthogonality check, because the associated mass and stiffness matrices are not considered in the calculation of the MAC value. The MAC value is calculated by the following equation from reference 15:

$$MAC = \frac{\left| \sum_{j=1}^m \psi_1^*(j) \psi_2(j) \right|^2}{\sum_{j=1}^m [\psi_1^*(j) \psi_1(j)] \sum_{j=1}^m [\psi_2^*(j) \psi_2(j)]}$$

Although the MAC matrix is a very useful tool in performing mode shape correlation, user judgment is required, as contaminating effects such as geometric aliasing, nonlinearities, or noise may contribute to the calculation of erroneous MAC values. As pointed out in reference 16, the MAC value is only a measure of consistency, and not necessarily validation, between modal vector estimates. This is because the MAC cannot account for errors that may be consistent among all modal vector estimates.

## Analysis Models

The composite spars were modeled and analyzed with the MSC/NASTRAN finite-element program (ref. 17). Because each spar varied slightly with respect to the nominal wall thickness and weight prescribed for the spar type, a separate finite-element model was formed for each spar. With this approach, it was possible to more closely model each spar and account for individual variations than with a single model which has the averaged or "smeared" properties for each spar type. The finite-element models for each spar type are shown in figures 11 through 13. The structural modeling of each spar consisted of two-dimensional, quadrilateral flat plate (CQUAD4) elements having anisotropic properties. Although separate models were constructed for each spar, the same number of elements and grid points

was used for each model of a given spar type. All models were formed with 25 plate elements in the lengthwise direction, with the number of circumferential elements varying with cross-section type. (See appendix for results of a limited convergence study.) Eight plate elements were used circumferentially to model the square cross section, whereas 12 and 14 elements were used for the D-shape and elliptical geometries, respectively. The total degrees of freedom for each model were reduced through static condensation, with a reduced set of dynamic degrees of freedom resulting. The total number of grid points, as well as the number of plate elements and dynamic degrees of freedom for each model, is also listed in the associated figures. The plane of grid points for each model was located at the geometric midplane of the 4-ply laminate and was therefore coincident with the element reference plane. Structural mass was accounted for through the use of the consistent mass matrix option in the analyses. The nonstructural mass and associated inertia of the accelerometer mounting blocks attached to each spar were accounted for through the use of concentrated mass elements and solid elements. Concentrated mass (CONM2) elements were used to model the small impact blocks used for excitation input on the elliptical and D-shape spars, which used two blocks and one block, respectively. The accelerometer mounting block used on the square and D-shape spars was modeled with a single (CHEXA) solid element. The mounting block used on the elliptical spars was modeled by using four (CPENTA) solid elements.

## Results

### Experimental Results

**D-shape spar.** Although three D-shape spars (VD1, VD2, and VD3) were fabricated for this investigation, some anomalies were encountered in the testing and modal analyses for two of the three spars (VD2 and VD3). The cause of these anomalies, which were manifested as multiply-split poles and frequency shifts, could not be explained satisfactorily, although it may be likely due to material or lamination defects within the spars in question. Therefore, the two suspect spars were not considered further in the investigation and results are not presented for these spars.

The multivariate mode indicator function for the VD1 spar was calculated over the frequency range from 0 to 2000 Hz, where the driving point coherence exhibited the best characteristics and is shown in figure 14. Considering the relative magnitudes of the primary minima, approximately 15 modes appeared

to be within the range of interest. Although there is no threshold value which explicitly defines a minima as a potential mode, those minima occurring within the lower third of the value scale may generally be considered valid in this example. Minima occurring near this limit and above may also be considered although user judgment is required within this "gray area" in light of the rather ragged quality of the primary function, particularly in the frequency range from 0 to 300 Hz. This raggedness is most likely due to low coherence values which were observed in the cross measurements involving the axial ( $x$ ) measurements in this range. Apparent double-peaked minima occurring in the mid to upper ranges of the scale, as well as the slight drops in the secondary function, may likely be influenced by slight differences or shifts in frequency which were sometimes observed between measurement locations. No significant evidence of repeated roots was found, which would be manifested by substantial and coincident drops in the secondary and possibly tertiary functions in the graph.

With the information obtained from the MMIF, the analytical curve fit of the experimental data was performed by using the polyreference technique. The resulting synthesized frequency response function, plotted as an overlay on the experimental frequency response function, is shown in figure 15. The analytically synthesized function is nearly identical to its experimental counterpart throughout the frequency range from 0 to 2000 Hz, with the exception of the mode or modes near 1950 Hz. The phase has deteriorated considerably in this frequency range; this results in diminished accuracy in the analytical function. The corresponding frequency and mode shape data extracted from the polyreference curve fit in the real domain are listed in table 11, including the estimates of damping, phase angle, amplitude, and MCF. (Modal parameters were also obtained with the polyreference curve fit in the complex domain and did not differ significantly from those obtained in the real domain.) Thirteen modes were extracted within the frequency range from 0 to 2000 Hz. (Although the MMIF indicated potential modes occurring near 1850, 1925, and 1980 Hz, these minima were determined to correspond to local and/or frequency-shifted data and could not be captured by curve fits in a global or reduced bandwidth.) Of these 13 modes, 5 global "nonshell" modes, which are the primary mode types of interest, were identified: first vertical bending, first lateral bending, second vertical bending, first torsion, and second lateral bending. The mode shapes were scaled to the 1Z-driving point measurement. Because a frequency response function is a complex quantity (frequency

plus a real and an imaginary part), a set of multiple plots is required to completely represent the frequency response function because to fully describe it is not possible when using a single two-dimensional plot. One method of presenting the frequency response data involves plotting the real and the imaginary parts of the function versus frequency. This type of plot illustrates how the phase changes through a resonance, which is defined as the point where the real part is zero and the imaginary part has a maximum value. The magnitude of the frequency response function is equivalent to the square root of the sum of the squares of the real and imaginary parts. An additional plot associated with frequency response measurements is the coherence, which can be thought of as a ratio of signal to noise. The coherence represents a measure of the causality between the input and response signals and is always less than or equal to unity. A more in-depth discussion of these plots, including the mathematical basis, can be found in reference 18. Plots of the  $1Z_-$  driving point measurement are shown in figure 16 using the plot types described above. The global mode shapes are plotted in figure 17, with the dashed outline representing the undeformed shape. Because the grid points along the leading edge of the D-shape spar were not impacted in the vertical ( $Z$ ) direction, they appear undeformed in the plotted mode shapes. This is particularly evident in the mode shapes which have primarily vertical bending motions. Therefore, this incongruity must be considered when correlating the test and analysis mode shapes. The bending deformations of the D-shape spar appear slightly coupled with respect to the vertical ( $X-Z$ ) and lateral ( $X-Y$ ) planes. This coupling is a result of the parasitic bending-shear coupling which is inherent in an extension-twist-coupled laminate design. Bending-shear coupling influences a structure such that a shear deformation in a given plane is due to a bending deformation in an orthogonal plane. With the first lateral bending case (fig. 17(b)) as an example, a slight (secondary) deformation in the  $X-Z$  plane is observed in response to the primary bending deformation in the  $X-Y$  plane. This effect is observed in each of the bending mode cases, where the secondary deformation appears to assume a shape characteristic of the next higher bending mode (i.e., a slight second bending-type deformation is observed in the secondary plane in response to a first bending-type deformation in the primary plane). Also, the node points (points of zero displacement) are slightly asymmetric with respect to the center of the beam. This is because the application of the aluminum block at one end of the spar has shifted the beam mass center. Since this promotes a global change in the

beam mass distribution, this asymmetry will therefore exist in all observed modes. The shape of the first torsion mode (fig. 17(d)) is masked by the lack of participation of the leading-edge grid points in the vertical direction; therefore the determination of the mode shape is complicated. A torsion deformation is apparent in the vertical ( $X-Z$ ) plane with the change of phase between the right and left halves of the spar (with respect to the center). The lateral ( $X-Y$ ) plane perspective shows a slight lateral bending deformation over the grid points closest to the coordinate system origin. In this view, the mode shape assumes more of a vertical shearing characteristic than a torsional one.

**Square spars.** The experimental results for the square tubes (VS1, VS2, and VS3) are presented in this section. The multivariate mode indicator function is presented for each of the three square spars in figures 18, 19, and 20, respectively. In each case, the MMIF plots exhibited very similar characteristics and indicated approximately 10 modes within the frequency range from 0 to 2000 Hz for VS1 and VS3, although an 11th shell-type mode was apparent for VS2. Although several closely spaced modes were apparent, there was again no evidence of repeated or coincident roots. The synthesized frequency response function for VS1 is plotted with the associated experimentally derived function in figure 21. Overall, a very good fit was obtained throughout the range from 0 to 2000 Hz, with peaks as well as valleys accurately reproduced. Ten modes were extracted for VS1 and are listed in table 12. The mode shapes were scaled to the  $1Z_-$  driving point measurement, which is shown in figure 22. Five global modes were identified for VS1: first vertical bending, first lateral bending, second vertical bending, second lateral bending, and first torsion. The experimental mode shapes are illustrated in figure 23. The first vertical and lateral bending modes appear slightly coupled with their respective orthogonal planes such that the first mode bending deformation was apparent in both planes because the cross-sectional axes about which bending occurred were canted roughly  $20^\circ$  from the true vertical and lateral axes, respectively. The inertial asymmetry produced by the accelerometer block is fostering this effect, as the bending deformations would be otherwise uncoupled. (This was analytically confirmed by removing the block in the finite-element model and recalculating the mode shapes. No evidence of this coupling action was apparent in the recalculated mode shapes.) The first vertical and lateral bending modes appear uncoupled with respect to torsional deformation. However, it is noted that some torsional deformation is present in each of the

second bending modes. This coupled behavior is believed to be a function of the aforementioned inertial asymmetry because the spar is not structurally bending-twist coupled by design. The first torsion mode was similarly influenced and exhibited a slight second bending-type deformation in the lateral plane.

The analytically synthesized frequency response function is plotted as an overlay on the experimental frequency response function for the VS2 spar in figure 24. Eleven modes were extracted for the VS2 spar, as listed in table 13. The mode shapes were scaled to the  $1Z_-$  driving point measurement, which is shown in figure 25. Five global modes were identified: four bending modes and one torsion mode. The experimental mode shapes are nearly the same as those of VS1 and are thus not shown.

The experimental and analytically synthesized frequency response functions are shown in figure 26 for the final square spar, VS3. Ten modes were extracted within the frequency test range from 0 to 2000 Hz and are listed in table 14. These mode shapes were also scaled to the  $1Z_-$  driving point measurement shown in figure 27. As with the other two square spars, four global bending modes and the torsion mode were identified for VS3. The experimental mode shapes for VS3 were again similar to those obtained from VS1 and are not shown.

**Elliptical spars.** The test results for the three elliptical spars (VE1, VE2, and VE3) are presented in this section. The corresponding multivariate mode indicator functions for VE1, VE2, and VE3 are shown in figures 28, 29, and 30, respectively. Seven modes were evident within the frequency range from 0 to 2000 Hz for VE1, whereas six modes were evident for VE2 and VE3. Note the coincident drops in the secondary MMIF functions for VE2 and VE3, which appear to indicate coincident or repeated roots at the associated frequencies, given the somewhat significant magnitude of the minima.

The corresponding analytically synthesized frequency response function, as obtained from the polyreference curve fit, is plotted with the experimental frequency response function in figure 31 for the VE1 spar. In general, the curve fit exhibited very good characteristics within the frequency range from 0 to 2000 Hz although the antiresonance near 1750 Hz appeared slightly shifted between the test data and the analytical curve fit. Seven modes were determined in the frequency range from 0 to 2000 Hz for the elliptical spar and are listed in table 15. Although the MMIF function, shown in figure 28, indicated a potential occurrence of repeated roots within the frequency range, none were found. The mode

shapes were scaled to the  $1Z_-$  driving point response shown in figure 32. A significant deterioration in the coherence function was evident near 1600 Hz for the driving point response, perhaps affecting the quality of the curve fit in this region. Five global modes were identified for VE1 within the frequency range from 0 to 2000 Hz: first vertical bending, first lateral bending, second vertical bending, second lateral bending, and first torsion. The experimental mode shapes for VE1 are shown in figure 33. The bending modes are classical in nature and are not coupled to torsional deformation. The effects of the parasitic bending-shear coupling are again evident in the bending modes. The grid points lying on the upper surface of the elliptical spar (grid points 1–6) did not receive a lateral excitation and therefore appear undeformed. The first torsion mode exhibits a slight coupling motion in the vertical ( $Z$ ) plane such that a near second bending deformation is manifested. A sixth global mode characteristic of third vertical bending was strongly evident in the mode at 1865.52 Hz, shown in figure 33(f).

The synthesized and experimental frequency response functions for the VE2 spar are plotted in figure 34. The overall agreement is very good in the frequency range from 0 to 2000 Hz. Six modes were extracted from the polyreference curve fit, with no evidence of repeated roots, and are listed in table 16. Five global modes were identified, with similar shape and modal characteristics as compared with VE1, and were scaled to the  $1Z_-$  driving point measurement shown in figure 35. A sixth global mode characteristic of third vertical bending was evident in the mode corresponding to 1739.82 Hz. The experimental mode shapes are not shown because of their similarity with those of VE1.

The analytically synthesized and experimental frequency response functions are shown in figure 36 for the VE3 spar. Once again, the magnitude and phase is very good throughout the frequency range from 0 to 2000 Hz, with excellent representation of all peaks and phase changes. The modal properties were subsequently determined for VE3, where six modes were determined in the frequency range from 0 to 2000 Hz. The resulting parameters for the six modes are listed in table 17. The  $1Z_-$  driving point measurement for VE3 was used to scale the mode shapes and is shown in figure 37. Five global modes, similar to those obtained for VE1 and VE2, were identified. Additionally, the mode at 1838.58 Hz appeared to be characteristic of third vertical bending.

## Analytical Results

**D-shape spar.** The results from the normal modes and natural frequency analysis of the MSC/NASTRAN finite-element model of VD1 are listed in table 18 for the frequency range from 0 to 2000 Hz. The calculated frequencies which correspond to the global modes identified in the experiment are indicated in table 18. The corresponding mode shapes are illustrated in figure 38. Deformation of the cross sections adjacent to the accelerometer block is apparent for most of the analytical mode shapes. The magnitude of this deformation is greatly exaggerated in the figure because of the scaling of the plot. Also, the solid element appears to be stretching or deforming in the global mode shapes, but this is again an artifact from the plot scaling. Local boundary effects between the block and the plate element may further contribute to this distorted deformation. In order to more accurately capture the specific cross-sectional deformation, an increase in the number of plate elements around the circumference of the spar would be necessary. The calculated global bending modes are similar in shape to those obtained experimentally. The second vertical and lateral bending modes exhibit a slight torsional deformation, particularly evident along the leading edge of the D-shape, which is not apparent in the first bending modes. The torsional characteristic in the mode at 1254.97 Hz is very evident in figure 38(d), where most of the deformation occurs along the leading edge. This is expected based on an anticipated increase in the structural stiffness near the corners of the D-shape. Conversely, the torsional deformation is slightly coupled to a second vertical bending-type deformation, especially when viewed in the  $X$ - $Z$  plane.

**Square spars.** The frequencies obtained from a normal modes analysis for the square spars (VS1, VS2, and VS3) are shown in table 19 for the frequency range from 0 to 2000 Hz. The frequencies corresponding to global modes are indicated in the table. The mode shapes for VS1 are depicted in figure 39.

The first vertical and lateral bending modes of the square spars are classical in nature and do not appear to be significantly affected by the inertia of the accelerometer block. The second vertical ( $Z$ ) bending mode is only slightly affected by the associated cross-sectional deformation near the accelerometer block and this deformation is characteristic of a vertical shearing. In addition, the second bending modes are coupled to torsional deformation, perhaps as a result of the inertial asymmetry produced by the accelerometer block. The first torsion mode is apparent

at 1753.94 Hz and appears slightly coupled to second bending deformation.

The resultant analytical mode shapes for the VS2 and VS3 spars are nearly the same as those obtained for VS1 and are thus not shown.

**Elliptical spars.** The frequency and mode shape results for the elliptical spars (VE1, VE2, and VE3) are listed in table 20. The global mode shapes are indicated. The calculated mode shapes for VE1 are shown in figure 40.

The first vertical and lateral bending modes exhibit classical bending behavior, with little cross-sectional deformation. The same is generally true of the second vertical and lateral bending modes, although these modes appear to be slightly coupled with torsional deformation; this could be due to the asymmetrically mounted accelerometer blocks. In addition, the first two cross sections in the analytical model appear somewhat flattened, although the magnitude of this deformation is a function of scaling and is indeterminate. The first torsion mode, shown in figure 40(e), exhibits a slight coupling with a second bending-type deformation. The exaggerated size of the cross section is again a function of the scaling.

The corresponding mode shapes calculated for the VE2 and VE3 spars are nearly the same as those obtained for VE1 and are thus not shown.

## Experimental and Analytical Correlation

As a means of facilitating test-analysis correlation, the analytical model geometries generated in MSC/NASTRAN for each spar were cross mapped onto the corresponding experimental model geometries. Grid points common to both models (within a specified geometric tolerance) were identified through a comparison of the spatial geometry between the test and analysis graphics models. This resulted in streamlined analytical models which could then be compared in a direct manner with the test models, thereby allowing a one-to-one comparison of grid point deformations.

**D-shape spar.** Because the grid points along the leading edge of the D-shape spar were not excited in the vertical direction, they appeared effectively constrained in this direction for each mode. Correspondingly, this lack of vertical deformation did not lend itself well to comparison with the associated analytical grid point deformations, which were free to move in the vertical direction, and thus degraded test-analysis correlation. To compensate for this, the vertical deformations of the associated analysis grid points were effectively negated for the cross-mapped

geometry model in the calculation of the MAC matrix for VD1. The analytical data sets containing the resultant deformations for the finite-element models were modified such that zero vertical deformation existed for the selected grid points. This permitted the analysis model to mimic the lack of vertical deformation at the prescribed grid points while being free from the constraining effects associated with an applied boundary condition. The resulting test-analysis MAC matrix for the D-shape spar is presented in figure 41. The matrix is shown in a three-dimensional perspective view as well as a two-dimensional view to aid in the distinction of the constituent matrix members. Excellent agreement was obtained for the first vertical bending, first lateral bending, and first torsion modes, which correspond to the (1,1), (2,2), and (5,5) test-analysis matrix members. The associated MAC values for these pairs were in the range from 0.8 to 1.0, as shown in table 21. The agreement between the test-analysis second vertical bending and second lateral bending modes was relatively fair, with MAC values of 0.565 and 0.484, respectively. The magnitude of these values seems somewhat low and is thought to be associated with slight differences in deformation characteristics for each mode. This is particularly evident in the comparison of the second lateral bending modes, where the analytical mode exhibits some torsional deformation which is not apparent in the test mode shape. Nevertheless, these modes have the characteristics of the second lateral bending shape and are judged to correspond to such. The additional modes, which correspond to the shell-type modes, occupy the remainder of the matrix and have MAC values from 0.0 to 0.8. It is noted that the MAC members corresponding to the test-analysis (7,1) and (1,6) matrix members have MAC values in the range from 0.6 to 0.8. In the former pair, the seventh test mode actually does resemble the first analysis mode (first vertical bending). However, geometric aliasing is promoting this elevated MAC value. In the latter pair, the first test mode (first vertical bending) is similar to the sixth analytical mode, which is a shell-type mode. This similarity occurs as a result of the modification of the vertical deformation in analytical grid points 7–12. Therefore, the cross-mapped model and the test model do appear similar in this mode, but this is clearly a consequence of compensating for the apparent immobilities of the test grid points and does not constitute a true agreement of mode shapes.

The overall agreement for the D-shape tube frequencies is good, generally ranging from 1.9 percent difference (first vertical bending case) to 13.8 percent difference (second vertical bending case). The

average difference between test and analysis frequencies is approximately 6.0 percent.

**Square spars.** The interpretation of the MAC matrices for the square spars was straightforward in that all test and analysis grid points already possessed the same degrees of freedom; therefore, no additional adjustments needed to be performed.

The test-analysis MAC matrix for VS1 is shown in figure 42. Excellent agreement is exhibited for the first three global bending modes (first vertical, first lateral, and second vertical bending), with associated MAC values ranging from 0.8 to 1.0, as listed in table 22. The second lateral bending mode, however, agrees poorly with its analytical counterpart, having a calculated MAC value of 0.243. A comparison of the test and cross-mapped analysis mode shapes, shown in figure 43, reveals that the two modes generally have the same shape. However, the cross-mapped analysis model is lacking the torsional deformation of the grid points farthest from the origin which is present in the test. This appears to be the only significant difference between the two mode shapes, and it was therefore concluded that the test and analysis mode shapes do correspond, although some uncertainty exists. The first torsion mode from the test was found to agree fairly well with its analytical counterpart and had a MAC value of 0.573. Although the agreement of test-analysis data for VS1 was within 9.5 percent difference (second lateral bending), the average frequency difference was approximately 7.3 percent, with the best-case (first lateral bending) showing a 5.8 percent difference between test and analysis data.

The test-analysis MAC matrix for VS2 is shown in figure 44. Excellent agreement between test and analysis mode shapes is again evident for the first three global bending modes (first vertical bending, first lateral bending, and second vertical bending), and the associated MAC values are listed in table 23. The second lateral bending mode shape correlated poorly with that obtained from the analysis, having a MAC value of 0.347. The analytical torsion mode (1753.94 Hz) showed roughly equal MAC values with the 1550.65-Hz test mode (0.564) and the 1702.77-Hz test mode (0.531). By inspecting the plotted mode shapes further (fig. 45), the test mode at 1550.65 Hz was judged to be a closer match for the analytical mode in terms of overall mode shape characteristics.

Overall, the agreement between test and analysis frequencies was within 11.6 percent, with the best agreement corresponding to the first vertical bending mode (6.9 percent). The average difference between test and analysis data was approximately 8.9 percent.

The MAC matrix for the VS3 spar exhibited the best overall correlation of the square spars and is shown in figure 46. The MAC values corresponding to the global test and analysis pairs are listed in table 24. Excellent correlation was again obtained for the first three global bending modes, with the calculated MAC values ranging from 0.861 to 0.937. Comparison of the test and analysis shapes for second lateral bending mode (fig. 47) involved two test modes which appeared to share similar characteristics with the analytical mode shape. The test mode at 1423.28 Hz showed favorable correlation with the analytical mode at 1555.08 Hz in terms of calculated MAC value (0.504). However, although the test mode corresponding to 1459.78 Hz shared similar shape characteristics with its analytical counterpart, the associated MAC value for this analysis and test pair was only 0.011. This would seem to indicate a total lack of correlation for the two mode shapes, although some similarities are apparent from figure 47. Based on the relative MAC values, the mode at 1423.28 Hz better approximated the analytical second lateral bending deformation. The respective test and analysis torsion modes correlated favorably, with a MAC value of 0.645.

The agreement between the global test and analysis frequencies was generally very good for the VS3 spar. The best agreement was found for the first lateral bending mode, showing a difference of only 2.3 percent. Although some uncertainty was observed regarding the test second lateral bending mode, the correlation between the test mode at 1423.28 Hz and the analytical mode exhibited higher MAC values and agreed within 8.5 percent. The average difference between test and analysis data was 4.4 percent.

***Elliptical spars.*** Similar to the VD1 spar, the cross-mapped analysis models for the elliptical spars were modified to compensate for the lack of lateral deformation of the corresponding test grid points. In this case, the lateral deformations for the upper row of grid points (grid points 1–6 in fig. 9(c)) were zeroed out, as these grid points did not experience lateral excitations in the test. The resultant test-analysis MAC matrix for the VE1 spar is shown in figure 48. Excellent correlation was obtained for the five global modes. These modes had MAC values from 0.820 to 0.980, as shown in table 25. The analytical mode shape corresponding to third vertical bending showed good correlation with the test mode at 1865.52 Hz, with a MAC value of 0.677.

The data correlation for the VE1 spar exhibited very good agreement with experiment, with

results ranging from 0.10 percent (first torsion) to 4.9 percent (second lateral bending) for the five modes. The average difference between test and analysis frequencies was about 2.5 percent.

The calculated MAC matrix for the VE2 spar is shown in figure 49. Excellent correlation was again obtained for the first four global modes. The associated MAC values, shown in table 26, ranged from 0.843 to 0.978 for these modes. The test-analysis correlation for the first torsion mode was good (MAC value of 0.753), whereas the analytical third vertical bending mode exhibited relatively poor correlation with the experimental mode at 1739.82 Hz (MAC value of 0.394).

In general, the test-analysis results for VE2 exhibited very good agreement. The agreement ranged from 1.9 percent difference (first vertical bending) to 7.7 percent (first lateral bending) for the five modes. The average difference between test and analysis data was approximately 4.8 percent.

The MAC matrix calculated for the third elliptical spar, VE3, is shown in figure 50. The matrix closely resembled those obtained for VE1 and VE2. Excellent agreement was obtained for the five global modes, with the calculated MAC values ranging from 0.800 to 0.980 as listed in table 27. The test-analysis correlation between the analytical third vertical bending mode and the experimental mode at 1838.58 Hz was good, with an associated MAC value of 0.712.

The agreement between test and analysis frequencies was generally very good and ranged from 1.6 percent (first vertical bending) to 9.6 percent (first lateral bending) for the first five modes. The average difference between test and analytical frequencies was approximately 6.0 percent.

## Concluding Remarks

Dynamic finite-element analyses of thin-walled composite tubular spars exhibiting extension-twist coupling have been conducted and compared with experimental data. The cross-sectional design of the spars corresponded to three types: square, D-shape, and elliptical. Because these designs were noncircular in nature, they were therefore prone to cross-sectional warping. Finite-element analysis models were constructed for each spar to account for individual variations in wall thickness and, thus, weight, which were present in each manufactured spar. Results from normal mode and frequency analyses of the finite-element models were compared with those obtained from free-free dynamic tests of the fabricated

spars. Five global or nonshell-type modes were identified for the D-shape spar in the frequency range from 0 to 2000 Hz: first vertical bending, first lateral bending, second vertical bending, first torsion, and second lateral bending. The agreement between test and analysis frequencies corresponding to the mode shapes was good, ranging from 1.9 percent (first vertical bending) to 13.8 percent (second lateral bending). The average difference for all modes was approximately 6.0 percent.

Five global modes were similarly extracted for each of three square spars (VS1, VS2, and VS3) in the frequency range from 0 to 2000 Hz. The identified mode shapes corresponded to first vertical bending, first lateral bending, second vertical bending, second lateral bending, and first torsion. The overall agreement between test and analysis results for the first square spar, VS1, was within 9.5 percent, with the best case agreement of 5.8 percent (first lateral bending). The average difference in the test and analysis frequencies was 7.3 percent. The test and analysis data correlation for VS2 ranged from 6.9 percent (first vertical bending) to 11.6 percent (first torsion), with the average difference calculated at 8.9 percent. The test-analysis correlation for the final square spar, VS3, agreed within 8.5 percent overall. The average difference was 4.4 percent.

Three elliptical spars were similarly tested and analyzed. Five global modes were obtained for each spar in the frequency range from 0 to 2000 Hz: first vertical bending, first lateral bending, second vertical bending, second lateral bending, and first torsion. The agreement between test and analysis frequencies for the VE1 spar ranged from 0.10 percent (first torsion) to 4.9 percent (second lateral bending) for the five global modes. The average difference between test and analysis frequencies was approximately 2.5 percent. Similar trends were observed for VE2, with agreement of test and analysis frequencies ranging from 1.9 percent difference (first vertical bending) to 7.7 percent (first lateral bending) for

the first five global modes. An average difference of 4.8 percent was observed between test and analysis frequencies. The agreement between test and analysis frequencies for VE3 ranged from 1.6 percent (first vertical bending) to 9.6 percent (first lateral bending) for the first five modes. The average difference between test and analytical frequencies was approximately 6.0 percent.

These results suggest that the structural dynamic characteristics of thin-walled composite structures employing extension-twist coupling can be determined within practical engineering accuracy. The fabrication process employed in this investigation has demonstrated the potential for achieving a high level of repeatability in the manufacturing of composite structures. Despite inconsistencies in the cured wall thicknesses of the elliptical spar subset, this method generally yielded spars of excellent overall geometric integrity. It is important to note that a certain level of experience with this type of fabrication process is required, as there are several variables unique to the rubber expansion method which directly control spar quality. Repeatability in the manufacturing process is essential for the reliable and efficient reproduction of composite structural components that will be incorporated in future rotorcraft systems. This investigation of tubular spars provides a necessary data base to promote understanding structural dynamic characteristics of elastically coupled composite rotor blade spars. Future studies of increased scope and complexity, including the investigation of the effect of large values of pretwist in elastically coupled structures, should further contribute to this data base and provide a basis for the development of practical composite tilt rotor blade designs incorporating extension-twist coupling.

NASA Langley Research Center  
Hampton, VA 23681-0001  
October 16, 1992

## Appendix

### Convergence Study Results

A convergence study of limited scope was initiated to verify the adequacy of the finite-element models. Specifically, the number of spanwise elements was varied from 16 to 33 to determine the effects upon the natural frequencies, particularly those corresponding to the higher modes. Because this investigation was primarily concerned with the global mode shapes (bending and torsion) and not the shell-type modes, the number of elements used circumferentially to model the cross section was not changed. The percentage of degrees of freedom retained in the analyses via static condensation was held at approximately 13 percent for each model per the recommendations outlined in references 19 and 20. The

convergence study was performed with the finite-element model of the square spar. The results of this study are shown in table 28 for four test cases designated by "Model  $j$ ," where  $j = 16, 20, 25$ , and 33 spanwise elements. The results indicated that the frequencies corresponding to the model using 25 spanwise elements differed by a maximum of 0.65 percent when compared with the model using 33 elements in the spanwise direction. Furthermore, the average difference between these two models was approximately 0.39 percent. If the characteristic shape of the global bending and torsion modes is similar among all spar types (i.e., number of elements necessary to properly define bending and torsional mode shapes), the conclusion can be made that the model using 25 elements in the spanwise direction was sufficient for this investigation.

## References

1. Bachau, Olivier A.; and Hong, Chang-Hee: Finite Element Approach to Rotor Blade Modeling. *J. American Helicopter Soc.*, vol. 32, no. 1, Jan. 1987, pp. 60-67.
2. Dowell, E. H.; and Traybar, J. J.: *An Experimental Study of the Nonlinear Stiffness of a Rotor Blade Undergoing Flap, Lag and Twist Deformations*. NASA CR-137969, 1975.
3. Minguet, Pierre; and Dugundji, John: Experiments and Analysis for Structurally Coupled Composite Blades Under Large Deflections. Part 2—Dynamic Behavior. *A Collection of Technical Papers, Part 4—AIAA/ASME/ASCE/AHS/ASC 30th Structures, Structural Dynamics and Materials Conference*, American Inst. of Aeronautics and Astronautics, Apr. 1989, pp. 1817-1827. (Available as AIAA-89-1366-CP.)
4. Kim, Taehyoun; and Dugundji, John: *Nonlinear Large Amplitude Vibration of Composite Helicopter Rotor Blade at Large Static Deflection*. TELAC Rep. 90-14 (Contract No. DAAL 03-87-K-0024), Dep. of Aeronautics and Astronautics, Massachusetts Inst. of Technology, July 1990. (Available from DTIC as AD A227 933.)
5. Hodges, Dewey H.; Atilgan, Ali R.; Fulton, Mark V.; and Rehfield, Lawrence W.: Dynamic Characteristics of Composite Beam Structures. *National Specialists' Meeting on Rotorcraft Dynamics—Proceedings*, American Helicopter Soc., 1989, pp. 1-16.
6. Abarcar, Rene B.; and Cunniff, Patrick F.: The Vibration of Cantilever Beams of Fiber Reinforced Material. *J. Compos. Mater.*, vol. 6, Oct. 1972, pp. 504-517.
7. Lake, Renee C.; and Nixon, Mark W.: *A Preliminary Investigation of Finite-Element Modeling for Composite Rotor Blades*. NASA TM-100559, USAAVSCOM TM-88-B-001, 1988.
8. Hodges, Robert V.; Nixon, Mark W.; and Rehfield, Lawrence W.: *Comparison of Composite Rotor Blade Models: A Coupled-Beam Analysis and an MSC/NASTRAN Finite-Element Model*. NASA TM-89024, AVSCOM TM 87-B-2, 1987.
9. Nixon, Mark W.: Analytical and Experimental Investigations of Extension-Twist-Coupled Structures. M.S. Thesis, George Washington Univ., May 1989.
10. HP VISTA User's Manual—Software Version B.02.10. Manual Part No. 35630-90020, Hewlett-Packard Co., c.1989.
11. I-DEAS<sup>TM</sup> Level 3—Tdas<sup>TM</sup>. *Test Data Analysis, Reference Manual*. Structural Dynamics Research Corp., c.1986.
12. HP Modal Data Manager User's Manual—Software Version B.02.10. Manual Part No. 35632-90003, Hewlett-Packard Co., c.1989.
13. Deblauwe, Filip; Brown, David L.; and Allemand, Randall J.: The Polyreference Time Domain Technique. *Proceedings of the 5th International Modal Analysis Conference*, Volume II, Union College, 1987, pp. 832-845.
14. Williams, Roger; Crowley, John; and Vold, Havard: The Multivariate Mode Indicator Function in Modal Analysis. *Proceedings of the 3rd International Modal Analysis Conference*, Volume I, Union College, 1985, pp. 66-70.
15. I-DEAS Test<sup>TM</sup> User's Guide. Structural Dynamics Research Corp., c.1990.
16. Allemand, R. J.; and Brown, D. L.: A Correlation Coefficient for Modal Vector Analysis. *Proceedings of the 1st International Modal Analysis Conference & Exhibit*, Union College, 1982, pp. 110-116.
17. MSC/NASTRAN User's Manual—MSC/NASTRAN Version 65. MSR-39, MacNeal-Schwendler Corp., Nov. 1985.
18. Ewins, D. J.: *Modal Testing: Theory and Practice*. Research Studies Press, Ltd., c.1986.
19. Gockel, M. A., ed.: *MSC/NASTRAN Handbook for Dynamic Analysis—MSC/NASTRAN Version 63*. MSR-64, MacNeal-Schwendler Corp., June 1983.
20. MSC/NASTRAN Dynamics—II, Seminar Notes. MacNeal-Schwendler Corp., Feb. 1987.

Table 1. Material Properties of T650-42/ERLX 1925-2  
Graphite-Epoxy Cloth

$E_{11}, E_{22}$ , lb/in <sup>2</sup>	11.65 × 10 <sup>6</sup>
$G_{12}$ , lb/in <sup>2</sup>	8.20 × 10 <sup>5</sup>
$\nu_{12}$	0.05
$\rho$ , lb/in <sup>3</sup>	0.056
$t_{\text{ply}}$ , in.	0.0075

Table 2. Spar Wall Thicknesses and Weight Data

Spar	Average wall thickness, in.	Maximum deviation, percent	Measured weight, lb
VD1	0.0300	0.0	0.1896
VD2	0.0307	2.3	0.1962
VD3	0.0300	0.0	0.1929
VS1	0.0304	1.3	0.1929
VS2	0.0304	1.3	0.1940
VS3	0.0300	0.0	0.1918
VE1	0.0348	13.8	0.1631
VE2	0.0322	6.8	0.1598
VE3	0.0328	8.5	0.1731

Table 3. Mounting Block Types and Weights

Block type	Weight, lb
Accelerometer mount (D-shape, squares)	0.0128
Accelerometer mount (ellipses)	0.0053
Impact mount (leading edge of ellipses)	0.0016
Impact mount (upper surface of ellipses)	0.0016

Table 4. VD1 Test Node Locations

Test node	Global coordinates ( $x, y, z$ )
1	(0.63, -1.23, 0.46)
2	(4.50, -1.23, 0.46)
3	(10.13, -1.23, 0.46)
4	(14.13, -1.23, 0.46)
5	(19.50, -1.23, 0.46)
6	(23.63, -1.23, 0.46)
7	(0.63, 0.38, 0.00)
8	(4.50, 0.38, 0.00)
9	(10.13, 0.38, 0.00)
10	(14.13, 0.38, 0.00)
11	(19.50, 0.38, 0.00)
12	(23.63, 0.38, 0.00)

Table 5. VS1 Test Node Locations

Test node	Global coordinates ( $x, y, z$ )
1	(0.63, -0.59, 0.59)
2	(4.50, -0.59, 0.59)
3	(9.38, -0.59, 0.59)
4	(14.13, -0.59, 0.59)
5	(19.50, -0.59, 0.59)
6	(22.88, -0.59, 0.59)
7	(0.63, 0.59, 0.59)
8	(4.50, 0.59, 0.59)
9	(9.38, 0.59, 0.59)
10	(14.13, 0.59, 0.59)
11	(19.50, 0.59, 0.59)
12	(22.88, 0.59, 0.59)

Table 6. VS2 Test Node Locations

Test node	Global coordinates ( $x, y, z$ )
1	(0.63, -0.59, 0.59)
2	(4.50, -0.59, 0.59)
3	(9.25, -0.59, 0.59)
4	(15.00, -0.59, 0.59)
5	(19.50, -0.59, 0.59)
6	(23.00, -0.59, 0.59)
7	(0.63, 0.59, 0.59)
8	(4.50, 0.59, 0.59)
9	(9.25, 0.59, 0.59)
10	(15.00, 0.59, 0.59)
11	(19.50, 0.59, 0.59)
12	(23.00, 0.59, 0.59)

Table 7. VS3 Test Node Locations

Test node	Global coordinates ( $x, y, z$ )
1	(1.00, -0.59, 0.59)
2	(4.50, -0.59, 0.59)
3	(10.13, -0.59, 0.59)
4	(13.75, -0.59, 0.59)
5	(19.50, -0.59, 0.59)
6	(23.00, -0.59, 0.59)
7	(1.00, 0.59, 0.59)
8	(4.50, 0.59, 0.59)
9	(10.13, 0.59, 0.59)
10	(13.75, 0.59, 0.59)
11	(19.50, 0.59, 0.59)
12	(23.00, 0.59, 0.59)

Table 8. VE1 Test Node Locations

Test node	Global coordinates ( $x, y, z$ )
1	(1.00, -0.31, 0.45)
2	(4.50, -0.31, 0.45)
3	(9.50, -0.31, 0.45)
4	(14.13, -0.31, 0.45)
5	(19.50, -0.31, 0.45)
6	(23.00, -0.31, 0.45)
7	(1.00, -0.63, 0.00)
8	(4.50, -0.63, 0.00)
9	(9.50, -0.63, 0.00)
10	(14.13, -0.63, 0.00)
11	(19.50, -0.63, 0.00)
12	(23.00, -0.63, 0.00)

Table 9. VE2 Test Node Locations

Test node	Global coordinates ( $x, y, z$ )
1	(1.00, -0.31, 0.45)
2	(4.75, -0.31, 0.45)
3	(9.50, -0.31, 0.45)
4	(14.50, -0.31, 0.45)
5	(19.75, -0.31, 0.45)
6	(23.00, -0.31, 0.45)
7	(1.00, -0.63, 0.00)
8	(4.75, -0.63, 0.00)
9	(9.50, -0.63, 0.00)
10	(14.50, -0.63, 0.00)
11	(19.75, -0.63, 0.00)
12	(23.00, -0.63, 0.00)

Table 10. VE3 Test Node Locations

Test node	Global coordinates ( $x, y, z$ )
1	(1.00, -0.31, 0.45)
2	(4.50, -0.31, 0.45)
3	(9.50, -0.31, 0.45)
4	(14.50, -0.31, 0.45)
5	(19.50, -0.31, 0.45)
6	(23.00, -0.31, 0.45)
7	(1.00, -0.63, 0.00)
8	(4.50, -0.63, 0.00)
9	(9.50, -0.63, 0.00)
10	(14.50, -0.63, 0.00)
11	(19.50, -0.63, 0.00)
12	(23.00, -0.63, 0.00)

Table 11. Experimental Modal Parameters From Real Domain  
Polyreference Curve Fit for VD1

Mode shape	Frequency, Hz	Damping, percent	Amplitude	Phase, deg	MCF
1	<sup>a</sup> 394.38	0.372	$7.82 \times 10^4$	-90.0	0.999
2	<sup>a</sup> 575.05	0.356	$5.65 \times 10^2$	90.0	1.000
3	<sup>a</sup> 904.19	0.515	$1.69 \times 10^4$	-90.0	0.998
4	1051.48	1.189	$1.56 \times 10^5$	-90.0	0.984
5	<sup>a</sup> 1175.92	0.444	$7.98 \times 10^4$	-90.0	0.999
6	1275.25	0.448	$2.61 \times 10^4$	-90.0	0.997
7	1385.92	0.445	$1.66 \times 10^5$	-90.0	1.000
8	1482.19	0.383	$1.29 \times 10^5$	-90.0	0.994
9	1545.31	0.381	$3.53 \times 10^4$	-90.0	0.979
10	<sup>a</sup> 1576.74	0.541	$8.51 \times 10^4$	-90.0	0.989
11	1769.89	0.549	$4.23 \times 10^4$	-90.0	0.962
12	1897.91	0.536	$2.70 \times 10^3$	90.0	0.979
13	1955.92	0.533	$1.33 \times 10^4$	90.0	0.992

<sup>a</sup>Global mode.

Table 12. Experimental Modal Parameters From Real Domain  
Polyreference Curve Fit for VS1

Mode shape	Frequency, Hz	Damping, percent	Amplitude	Phase, deg	MCF
1	<sup>a</sup> 464.05	0.360	$7.27 \times 10^4$	-90.0	1.000
2	<sup>a</sup> 486.27	0.462	$2.05 \times 10^4$	-90.0	0.999
3	994.51	0.665	$1.11 \times 10^4$	90.0	0.996
4	<sup>a</sup> 1260.92	0.437	$1.65 \times 10^5$	-90.0	0.999
5	1323.75	0.287	$2.96 \times 10^3$	-90.0	0.985
6	1374.06	0.230	$4.63 \times 10^2$	-90.0	0.998
7	<sup>a</sup> 1412.16	0.469	$1.11 \times 10^5$	-90.0	1.000
8	1435.64	0.268	$2.32 \times 10^5$	-90.0	0.999
9	1591.98	0.358	$8.80 \times 10^3$	-90.0	0.994
10	<sup>a</sup> 1615.24	0.394	$5.01 \times 10^3$	-90.0	0.999

<sup>a</sup>Global mode.

Table 13. Experimental Modal Parameters From Real Domain  
Polyreference Curve Fit for VS2

Mode shape	Frequency, Hz	Damping, percent	Amplitude	Phase, deg	MCF
1	<sup>a</sup> 465.12	0.334	$8.82 \times 10^5$	-90.0	1.000
2	<sup>a</sup> 478.51	0.423	$2.01 \times 10^5$	-90.0	0.999
3	929.53	0.346	$1.23 \times 10^4$	-90.0	1.000
4	<sup>a</sup> 1240.09	0.464	$2.57 \times 10^6$	-90.0	0.999
5	1267.61	0.311	$5.01 \times 10^3$	-90.0	0.995
6	1330.98	0.375	$2.27 \times 10^6$	-90.0	0.998
7	<sup>a</sup> 1390.62	0.415	$4.94 \times 10^3$	90.0	0.991
8	1478.98	0.350	$6.14 \times 10^2$	-90.0	0.993
9	<sup>a</sup> 1550.65	0.459	$4.94 \times 10^5$	-90.0	0.997
10	1582.19	0.295	$4.86 \times 10^3$	-90.0	0.983
11	1702.77	0.513	$1.10 \times 10^6$	-90.0	0.999

<sup>a</sup>Global mode.

Table 14. Experimental Modal Parameters From Real Domain  
Polyreference Curve Fit for VS3

Mode shape	Frequency, Hz	Damping, percent	Amplitude	Phase, deg	MCF
1	<sup>a</sup> 485.33	0.383	$8.47 \times 10^5$	-90.0	0.999
2	<sup>a</sup> 503.38	0.398	$2.34 \times 10^5$	-90.0	0.999
3	1005.10	0.362	$1.36 \times 10^5$	-90.0	0.998
4	<sup>a</sup> 1297.59	0.489	$2.73 \times 10^6$	-90.0	1.000
5	1367.69	0.396	$1.53 \times 10^6$	-90.0	0.999
6	1379.64	0.375	$1.15 \times 10^5$	-90.0	0.978
7	<sup>a</sup> 1423.28	0.311	$2.69 \times 10^5$	-90.0	0.988
8	1459.78	0.416	$9.16 \times 10^3$	-90.0	0.983
9	1608.94	0.309	$2.98 \times 10^5$	-90.0	0.981
10	<sup>a</sup> 1653.92	0.443	$1.51 \times 10^5$	-90.0	0.995

<sup>a</sup>Global mode.

Table 15. Experimental Modal Parameters From Real Domain  
Polyreference Curve Fit for VE1

Mode shape	Frequency, Hz	Damping, percent	Amplitude	Phase, deg	MCF
1	<sup>a</sup> 382.55	0.391	$1.26 \times 10^6$	-90.0	1.000
2	<sup>a</sup> 481.01	0.377	$1.42 \times 10^4$	-90.0	0.999
3	<sup>a</sup> 1034.56	1.417	$2.10 \times 10^6$	-90.0	0.999
4	<sup>a</sup> 1279.04	0.662	$1.95 \times 10^5$	-90.0	0.998
5	<sup>a</sup> 1613.54	0.602	$6.07 \times 10^5$	-90.0	0.998
6	1844.53	2.226	$3.35 \times 10^5$	-90.0	0.990
7	1865.52	0.729	$4.78 \times 10^6$	-90.0	0.987

<sup>a</sup>Global mode.

Table 16. Experimental Modal Parameters From Real Domain  
Polyreference Curve Fit for VE2

Mode shape	Frequency, Hz	Damping, percent	Amplitude	Phase, deg	MCF
1	<sup>a</sup> 375.25	0.555	$1.23 \times 10^6$	-90.0	0.998
2	<sup>a</sup> 464.87	0.395	$1.42 \times 10^4$	-90.0	0.999
3	<sup>a</sup> 1013.66	1.197	$2.11 \times 10^6$	-90.0	0.999
4	<sup>a</sup> 1244.94	0.624	$1.46 \times 10^5$	-90.0	0.996
5	<sup>a</sup> 1571.33	0.673	$1.43 \times 10^6$	-90.0	0.996
6	1739.82	0.750	$2.31 \times 10^6$	-90.0	0.987

<sup>a</sup>Global mode.

Table 17. Experimental Modal Parameters From Real Domain  
Polyreference Curve Fit for VE3

Mode shape	Frequency, Hz	Damping, percent	Amplitude	Phase, deg	MCF
1	<sup>a</sup> 378.46	0.594	$1.21 \times 10^6$	-90.0	0.994
2	<sup>a</sup> 457.75	0.487	$1.37 \times 10^4$	-90.0	0.988
3	<sup>a</sup> 1023.89	1.071	$2.37 \times 10^6$	-90.0	0.981
4	<sup>a</sup> 1233.83	0.600	$7.59 \times 10^4$	-90.0	0.995
5	<sup>a</sup> 1514.81	0.617	$1.91 \times 10^5$	-90.0	0.996
6	1838.58	0.655	$4.31 \times 10^6$	-90.0	0.985

<sup>a</sup>Global mode.

Table 18. Calculated Frequencies  
From Finite-Element Analysis  
for D-Shape Spar

Mode shape	VD1 frequency, Hz
1	<sup>a</sup> 402.03
2	<sup>a</sup> 596.24
3	<sup>a</sup> 1048.71
4	1200.44
5	<sup>a</sup> 1254.97
6	1469.82
7	<sup>a</sup> 1647.74
8	1695.49
9	1731.15
10	1914.47
11	2113.61
12	2423.44
13	2608.75

<sup>a</sup>Global mode.

Table 19. Calculated Frequencies From Finite-Element Analysis for Square Spars

Mode shape	Frequency, Hz, for—		
	VS1	VS2	VS3
1	<sup>a</sup> 499.82	<sup>a</sup> 499.82	<sup>a</sup> 499.08
2	<sup>a</sup> 516.02	<sup>a</sup> 516.02	<sup>a</sup> 515.54
3	1169.83	1169.83	1159.44
4	<sup>a</sup> 1345.26	<sup>a</sup> 1345.26	<sup>a</sup> 1343.50
5	1445.49	1445.49	1430.12
6	1543.60	1543.60	1524.07
7	<sup>a</sup> 1559.64	<sup>a</sup> 1559.64	<sup>a</sup> 1555.08
8	1581.47	1581.47	1562.83
9	<sup>a</sup> 1753.94	<sup>a</sup> 1753.94	<sup>a</sup> 1737.28
10	1844.37	1844.37	1827.15
11		2518.15	

<sup>a</sup>Global mode.

Table 20. Calculated Frequencies From Finite-Element Analysis for Elliptical Spars

Mode shape	Frequency, Hz, for—		
	VE1	VE2	VE3
1	<sup>a</sup> 383.30	<sup>a</sup> 382.71	<sup>a</sup> 384.46
2	<sup>a</sup> 504.56	<sup>a</sup> 503.69	<sup>a</sup> 506.16
3	<sup>a</sup> 1063.54	<sup>a</sup> 1061.99	<sup>a</sup> 1066.41
4	<sup>a</sup> 1344.87	<sup>a</sup> 1342.42	<sup>a</sup> 1349.48
5	<sup>a</sup> 1615.38	<sup>a</sup> 1611.57	<sup>a</sup> 1624.76
6	<sup>a</sup> 2143.16	<sup>a</sup> 2136.97	<sup>a</sup> 2153.91
7	2304.54	2279.08	2368.29

<sup>a</sup>Global mode.

Table 21. Calculated Modal Assurance Criteria Values  
for Global Test and Analysis Modes for VD1

Mode shape	Matrix element		Calculated MAC value
	Test	FEA	
First vertical bending	1	1	0.971
First lateral bending	2	2	0.941
Second vertical bending	3	3	0.565
First torsion	5	5	0.889
Second lateral bending	10	7	0.484

Table 22. Calculated Modal Assurance Criteria Values  
for Global Test and Analysis Modes for VS1

Mode shape	Matrix element		Calculated MAC value
	Test	FEA	
First vertical bending	1	1	0.921
First lateral bending	2	2	0.923
Second vertical bending	4	4	0.862
Second lateral bending	7	7	0.243
First torsion	10	9	0.573

Table 23. Calculated Modal Assurance Criteria Values  
for Global Test and Analysis Modes for VS2

Mode shape	Matrix element		Calculated MAC value
	Test	FEA	
First vertical bending	1	1	0.945
First lateral bending	2	2	0.944
Second vertical bending	4	4	0.801
Second lateral bending	7	7	0.347
First torsion	9	9	0.564

Table 24. Calculated Modal Assurance Criteria Values  
for Global Test and Analysis Modes for VS3

Mode shape	Matrix element		Calculated MAC value
	Test	FEA	
First vertical bending	1	1	0.936
First lateral bending	2	2	0.937
Second vertical bending	4	4	0.861
Second lateral bending	7	7	0.504
First torsion	10	9	0.645

Table 25. Calculated Modal Assurance Criteria Values  
for Global Test and Analysis Modes for VE1

Mode shape	Matrix element		Calculated MAC value
	Test	FEA	
First vertical bending	1	1	0.980
First lateral bending	2	2	0.930
Second vertical bending	3	3	0.918
Second lateral bending	4	4	0.826
First torsion	5	5	0.820
Third vertical bending	7	6	0.677

Table 26. Calculated Modal Assurance Criteria Values  
for Global Test and Analysis Modes for VE2

Mode shape	Matrix element		Calculated MAC value
	Test	FEA	
First vertical bending	1	1	0.978
First lateral bending	2	2	0.922
Second vertical bending	3	3	0.926
Second lateral bending	4	4	0.843
First torsion	5	5	0.753
Third vertical bending	6	6	0.394

Table 27. Calculated Modal Assurance Criteria Values  
for Global Test and Analysis Modes for VE3

Mode shape	Matrix element		Calculated MAC value
	Test	FEA	
First vertical bending	1	1	0.980
First lateral bending	2	2	0.899
Second vertical bending	3	3	0.930
Second lateral bending	4	4	0.800
First torsion	5	5	0.822
Third vertical bending	6	6	0.712

Table 28. FEA Convergence Study Results for Square Spar

Mode shape	Frequency, Hz, for—			
	Model 16	Model 20	Model 25	Model 33
1	501.50	500.43	499.82	499.02
2	516.68	516.68	516.02	515.15
3	1180.22	1172.67	1169.83	1165.72
4	1359.89	1349.09	1345.26	1336.50
5	1453.30	1447.39	1445.49	1441.86
6	1544.74	1542.56	1543.60	1538.11
7	1573.29	1562.94	1559.64	1550.91
8	1580.67	1581.17	1581.47	1575.51
9	1772.39	1759.15	1753.94	1746.49
10	1854.56	1846.46	1844.37	1833.26

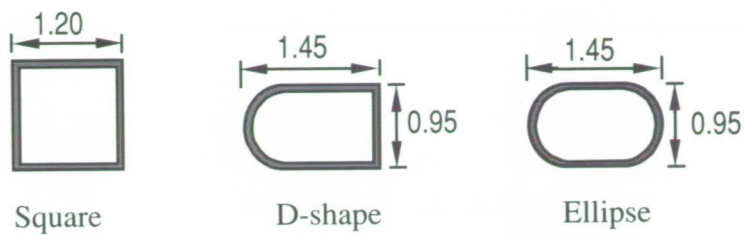


Figure 1. Cross-sectional designs for composite spars. Dimensions are in inches.

ORIGINAL PAGE  
BLACK AND WHITE PHOTOGRAPH

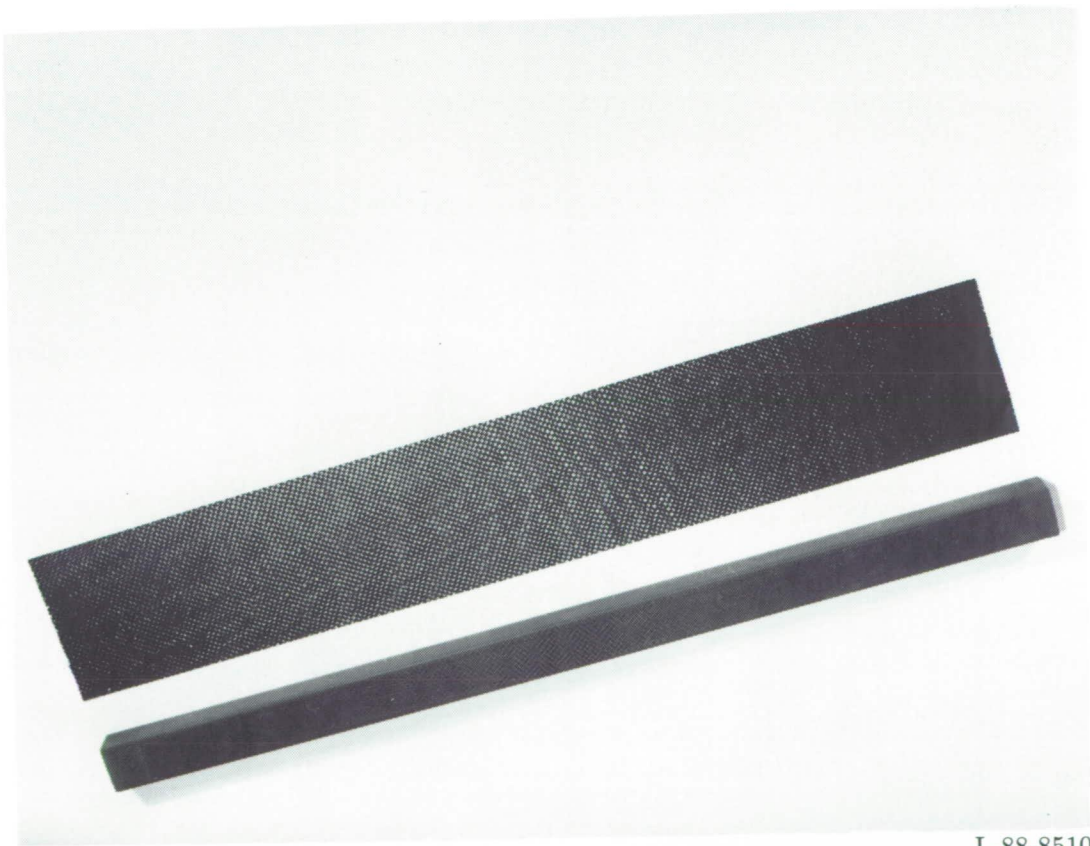
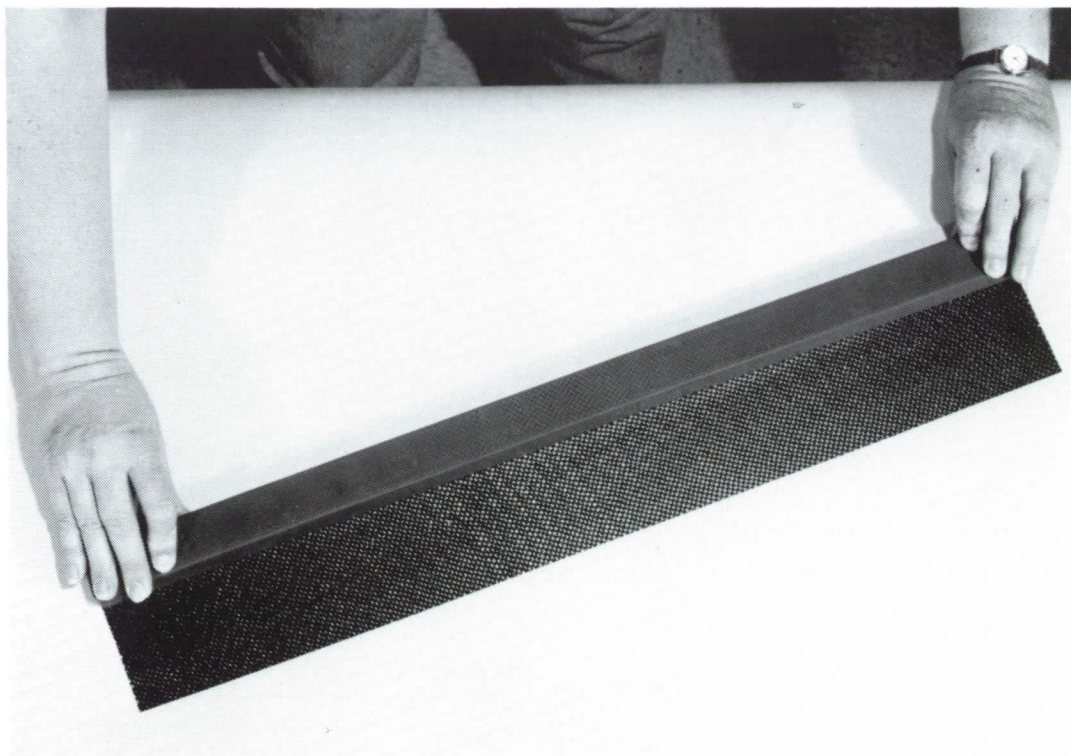


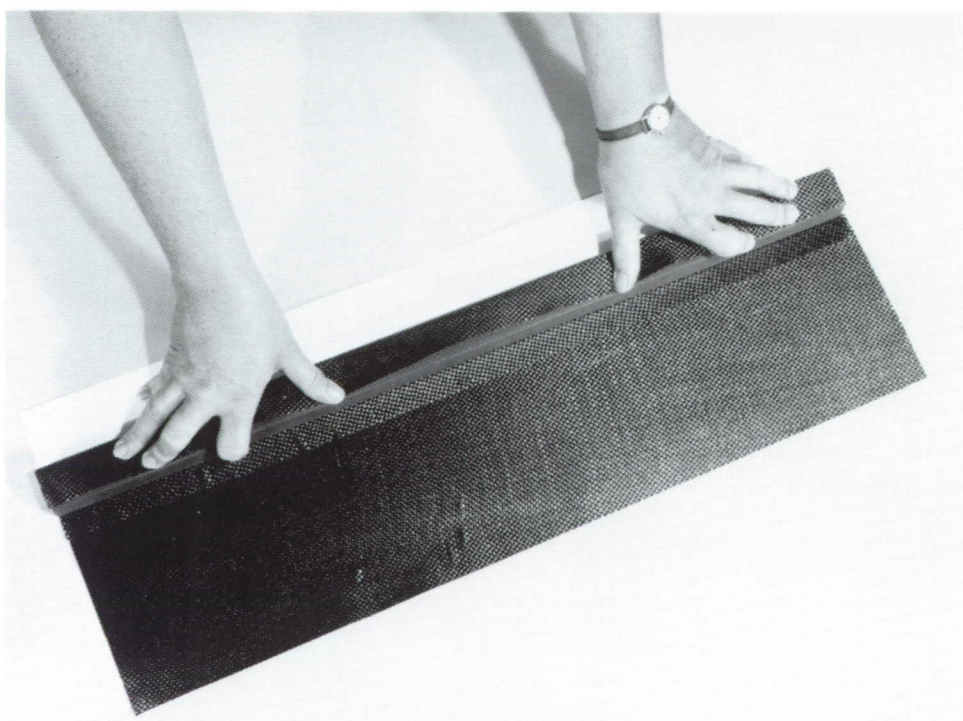
Figure 2. Initial composite mandrel wrap and silicon rubber tool.

ORIGINAL PAGE  
BLACK AND WHITE PHOTOGRAPH



L-88-8509

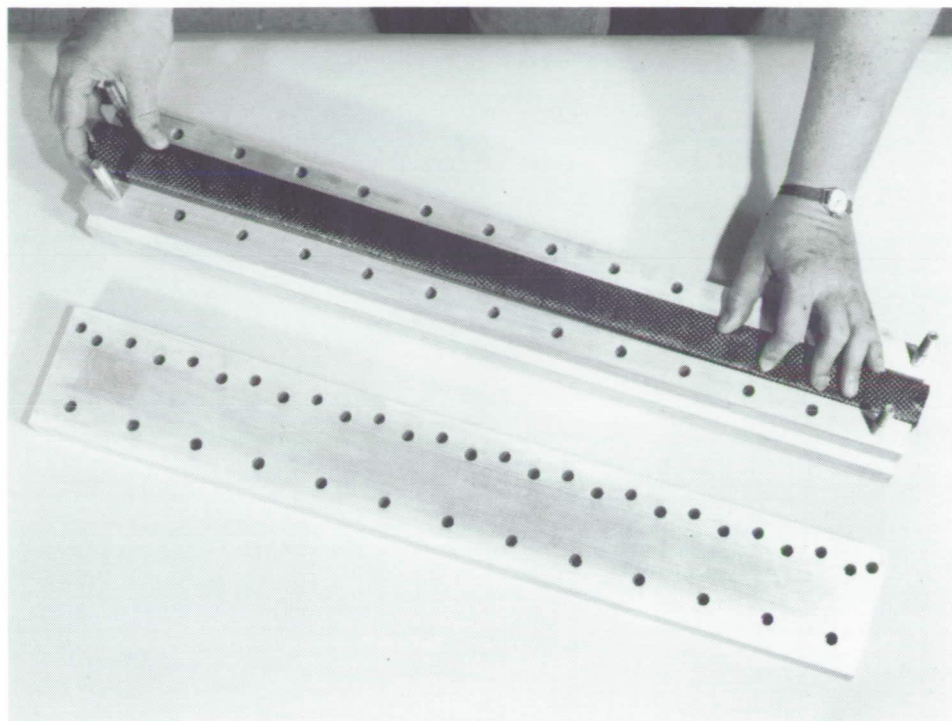
Figure 3. Initial wrapping of composite material.



L-88-8508

Figure 4. Continuation of wrap procedure using subsequent composite layers.

ORIGINAL PAGE  
BLACK AND WHITE PHOTOGRAPH



L-88-8506

Figure 5. Female aluminum tool cavity and cover plate.



L-88-11,779

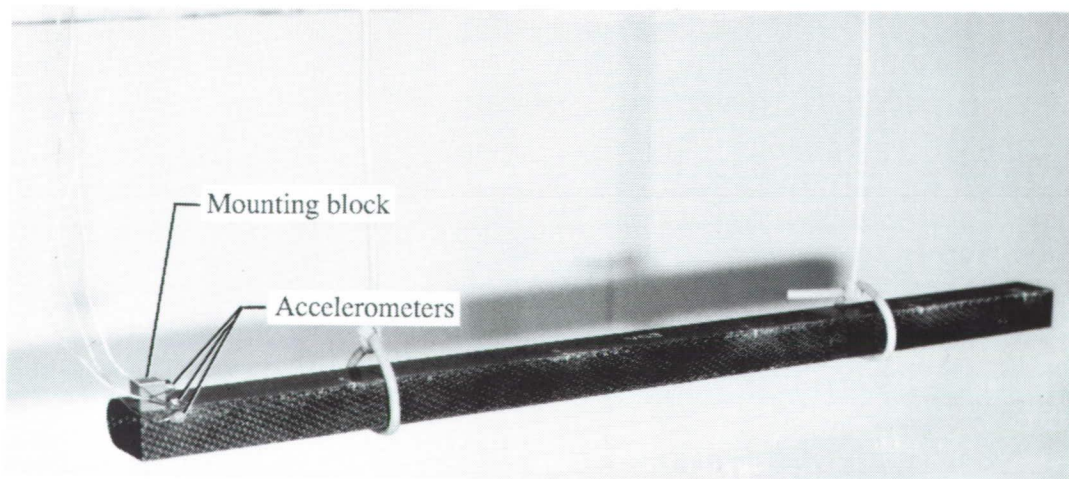
Figure 6. Cured tubular spars.

ORIGINAL PAGE  
BLACK AND WHITE PHOTOGRAPH



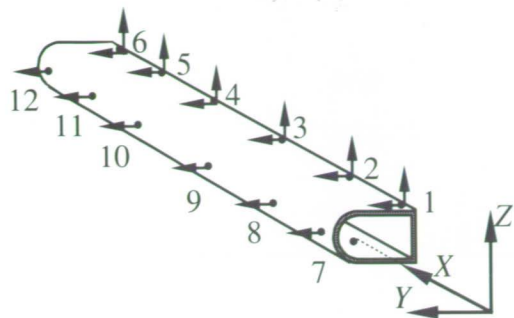
L-89-2511

Figure 7. Vibration test setup.

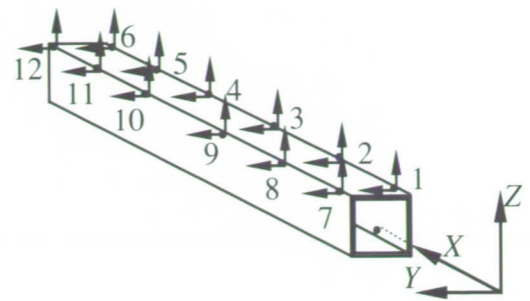


L-89-2513

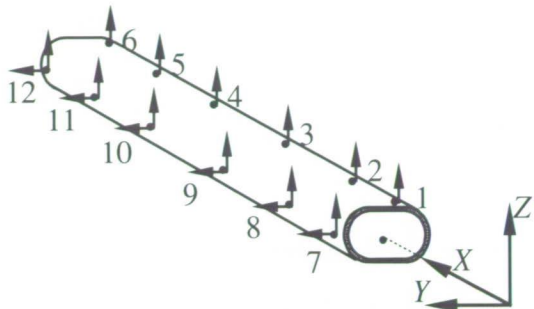
Figure 8. Triaxial accelerometer configuration.



(a) D-shape spar.

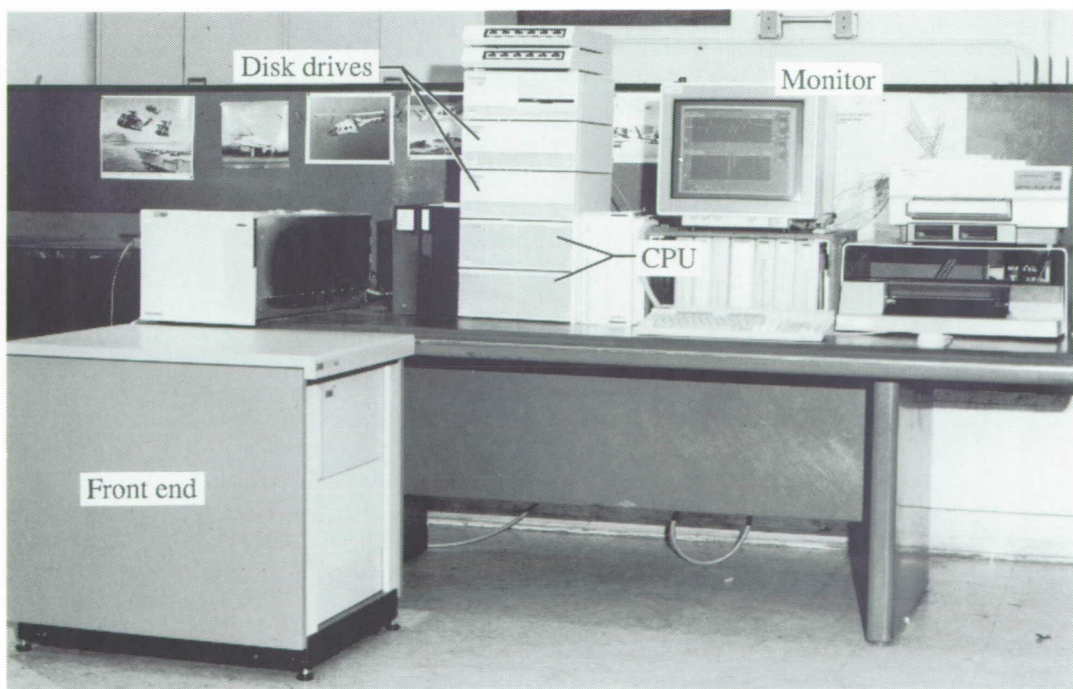


(b) Square spar.



(c) Elliptical.

Figure 9. Degrees of freedom for test spars.



L-89-2514

Figure 10. Data acquisition system.

ORIGINAL PAGE  
BLACK AND WHITE PHOTOGRAPH

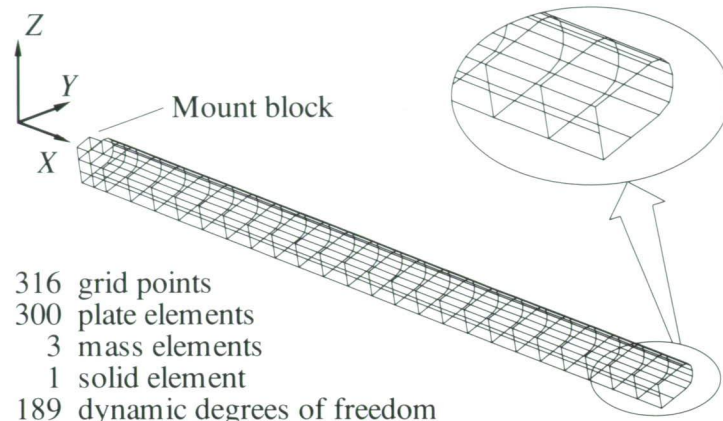


Figure 11. Finite-element model of D-shape spar.

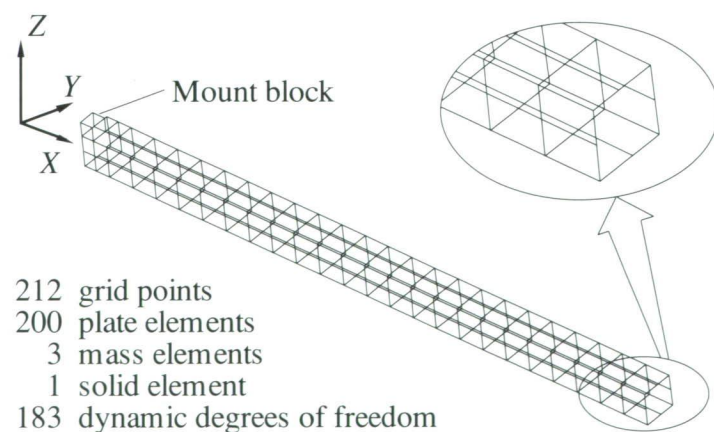


Figure 12. Finite-element model of square spar.

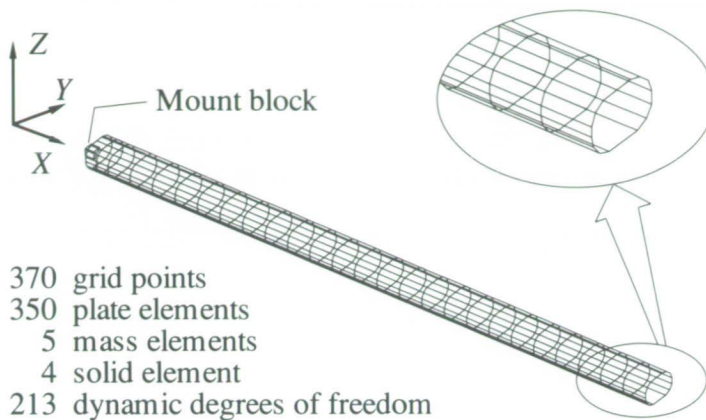


Figure 13. Finite-element model of elliptical spar.

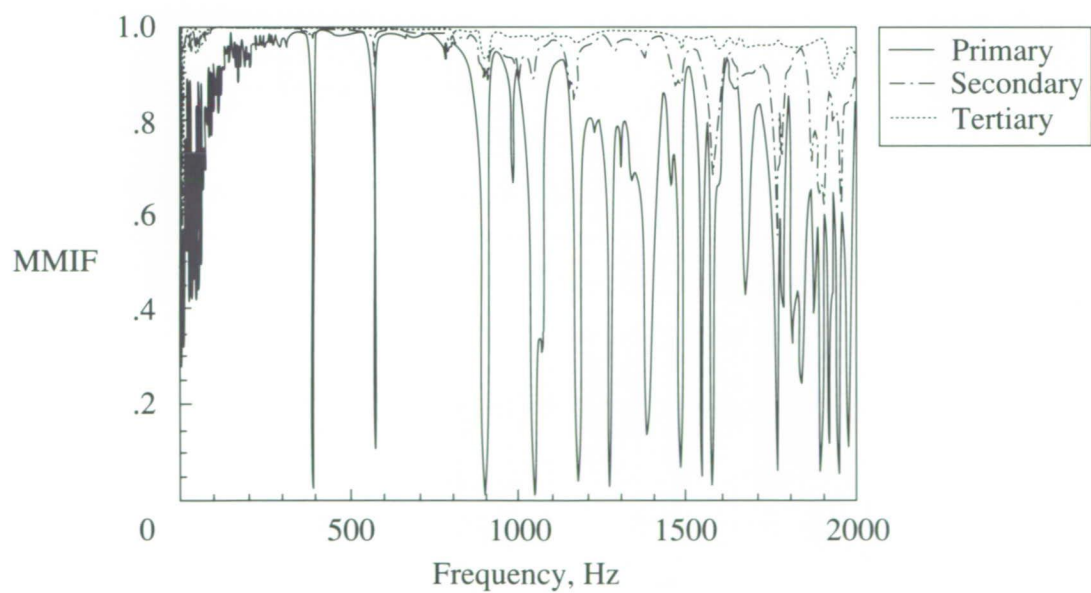


Figure 14. Multivariate mode indicator function for VD1.

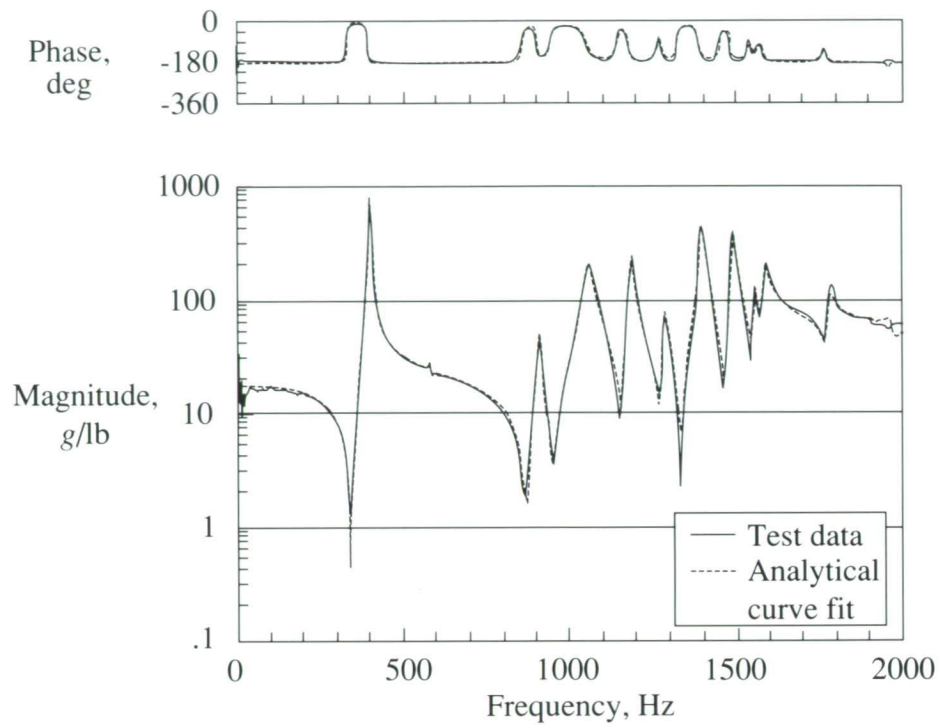


Figure 15. Frequency response function for VD1.

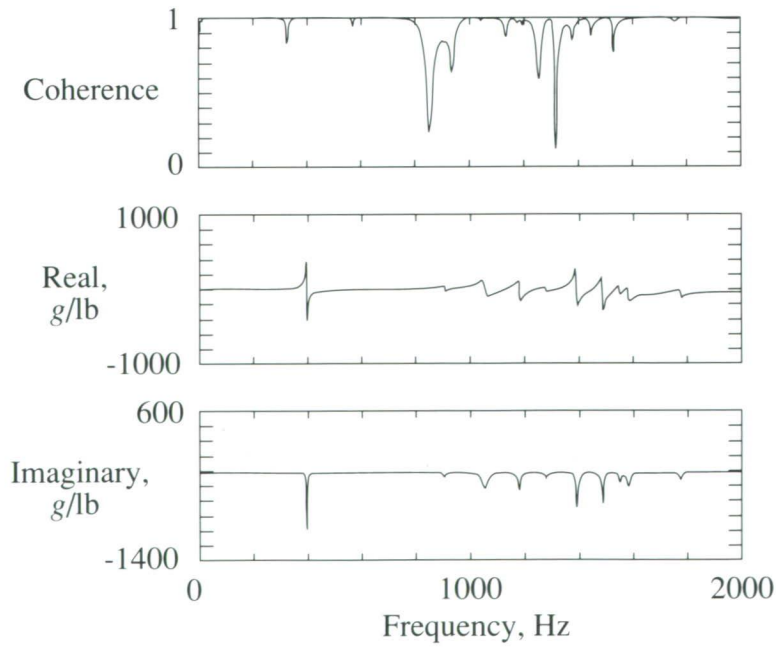
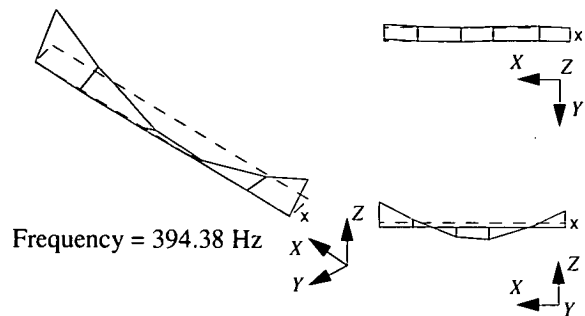
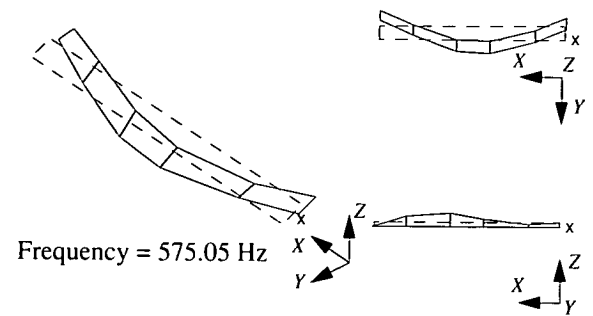


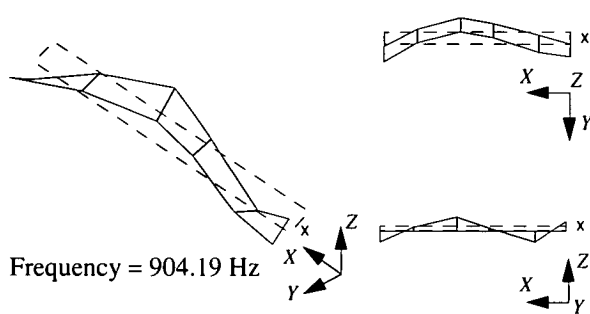
Figure 16.  $1Z_-$  driving point measurement for VD1.



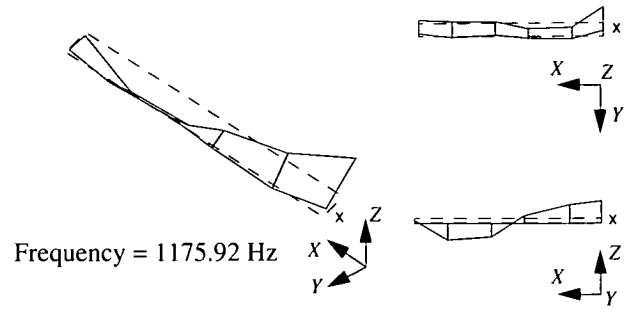
(a) First vertical bending.



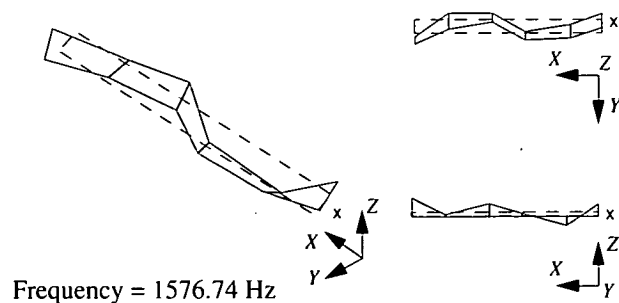
(b) First lateral bending.



(c) Second vertical bending.



(d) First torsion.



(e) Second lateral bending.

Figure 17. Global mode shapes for VD1.

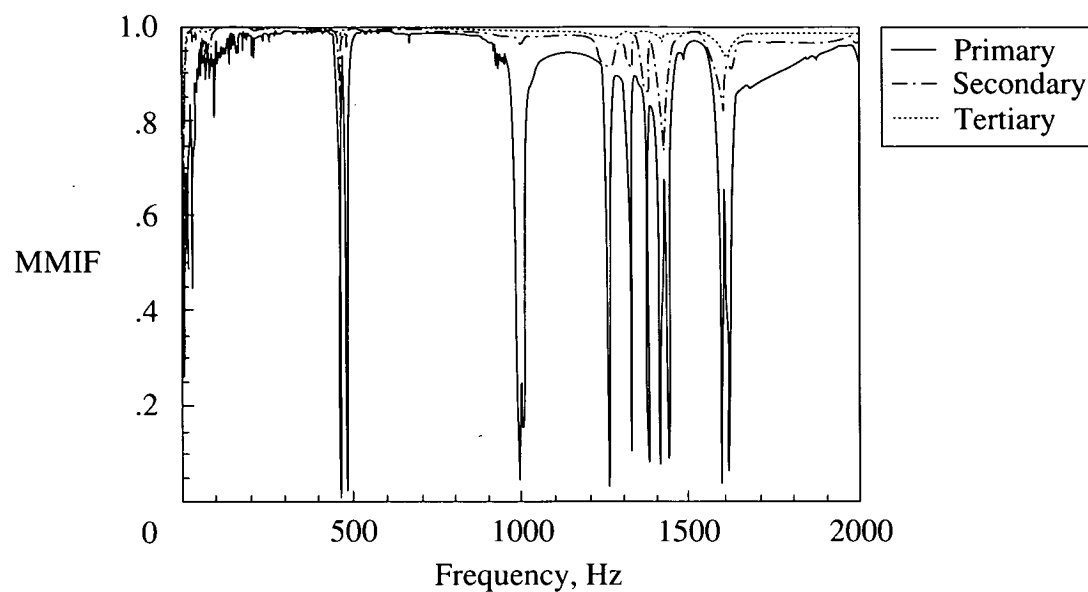


Figure 18. Multivariate mode indicator function for VS1.

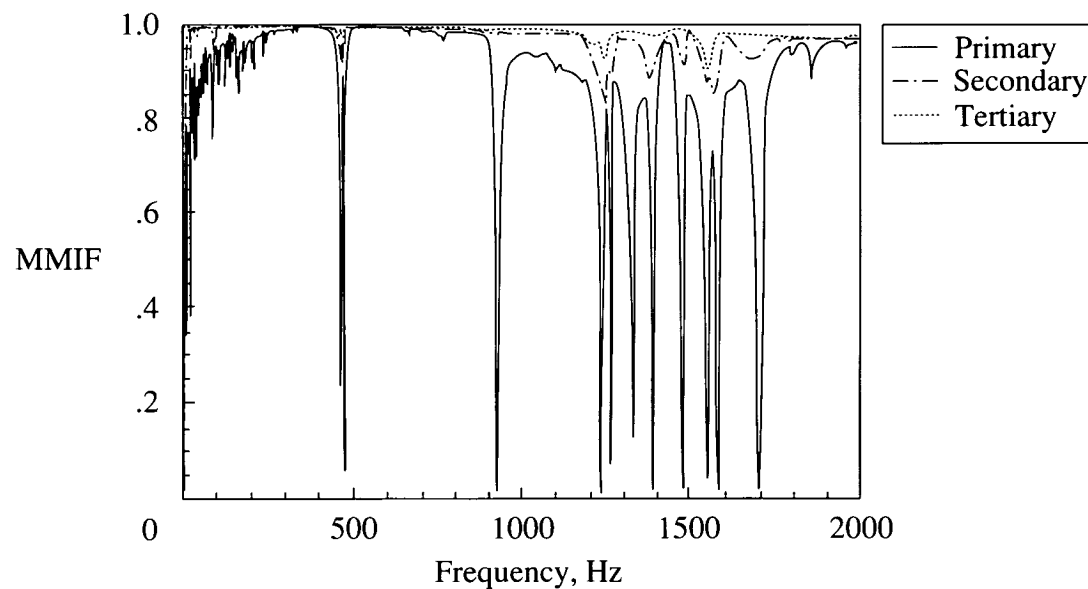


Figure 19. Multivariate mode indicator function for VS2.

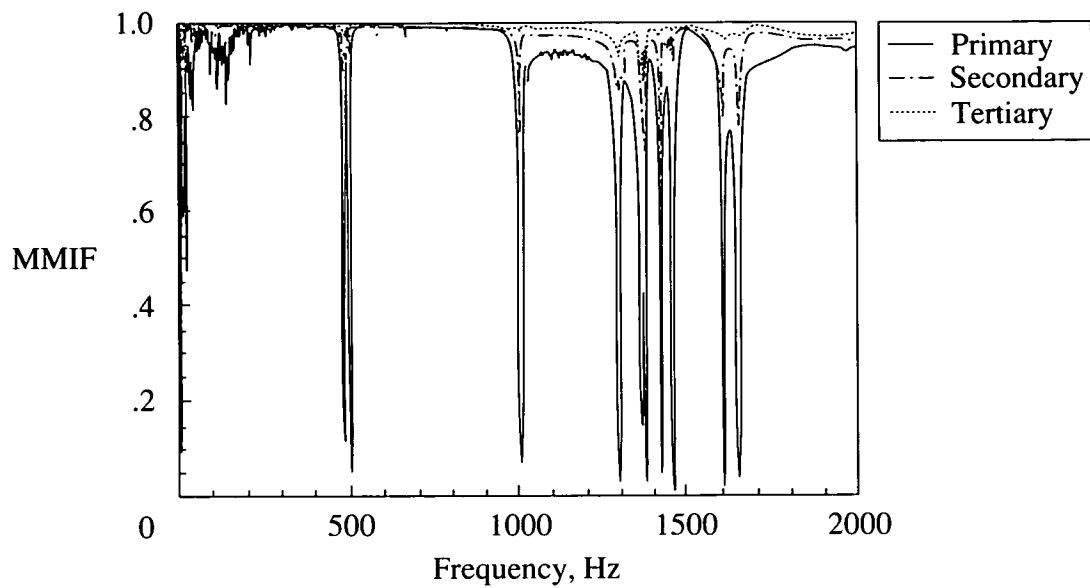


Figure 20. Multivariate mode indicator function for VS3.

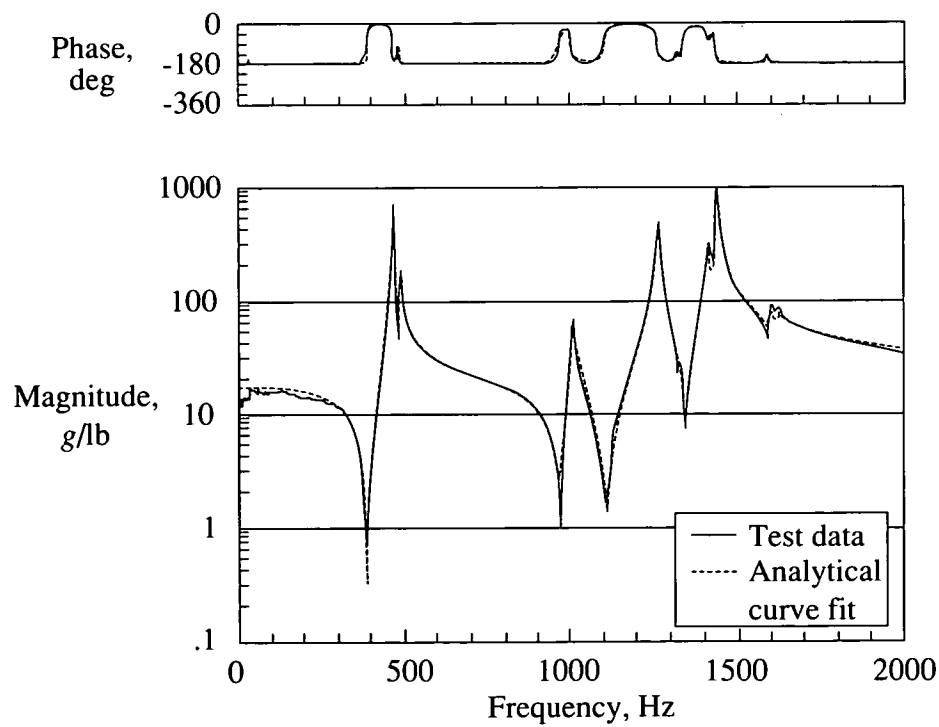


Figure 21. Frequency response function for VS1.

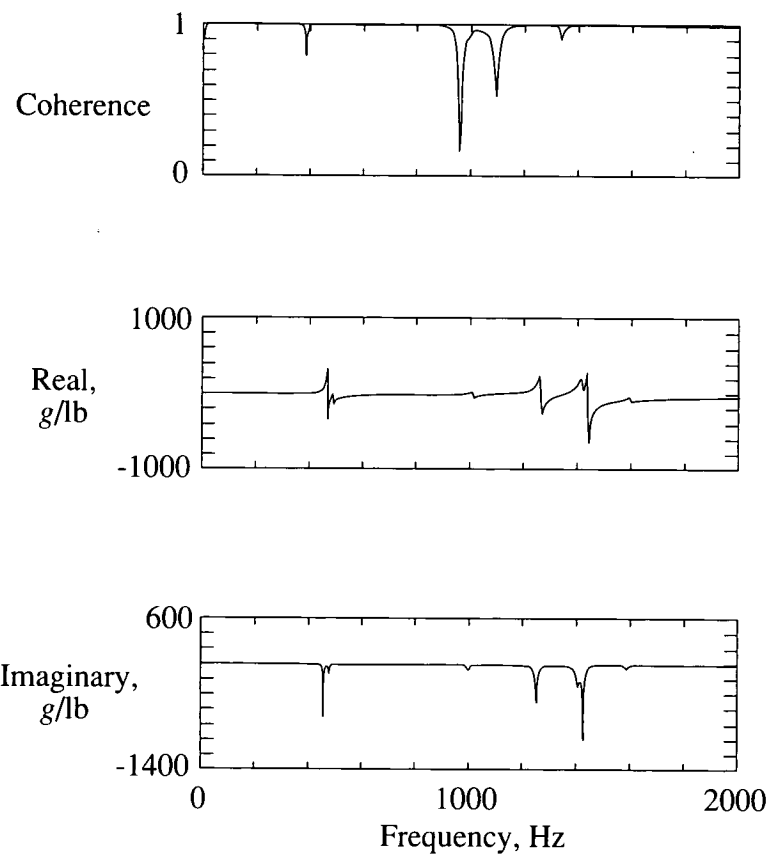


Figure 22.  $1Z_-$  driving point measurement for VS1.

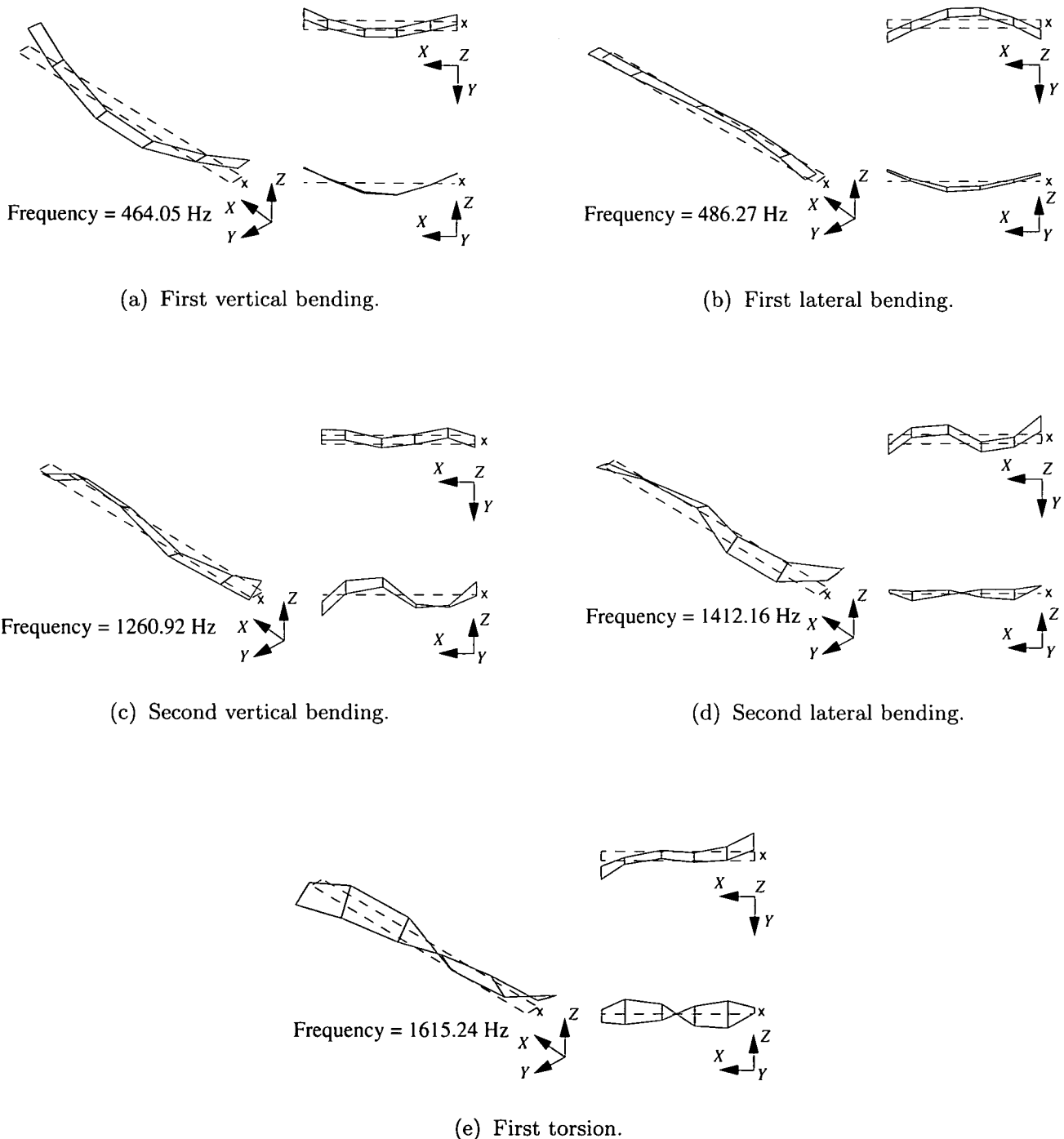


Figure 23. Global mode shapes for VS1.

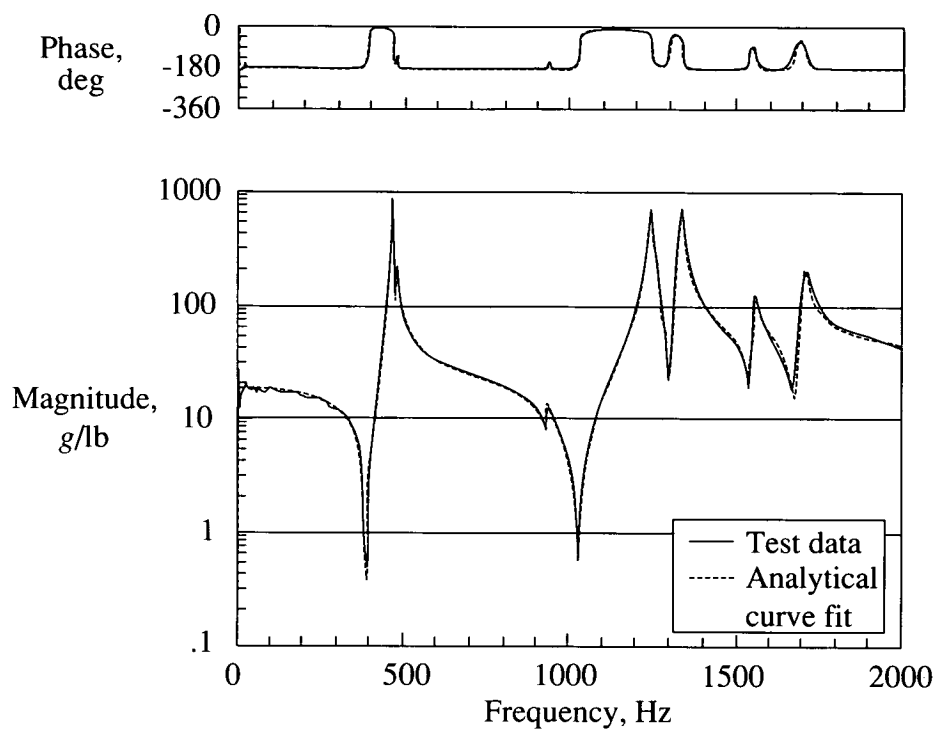


Figure 24. Frequency response function for VS2.

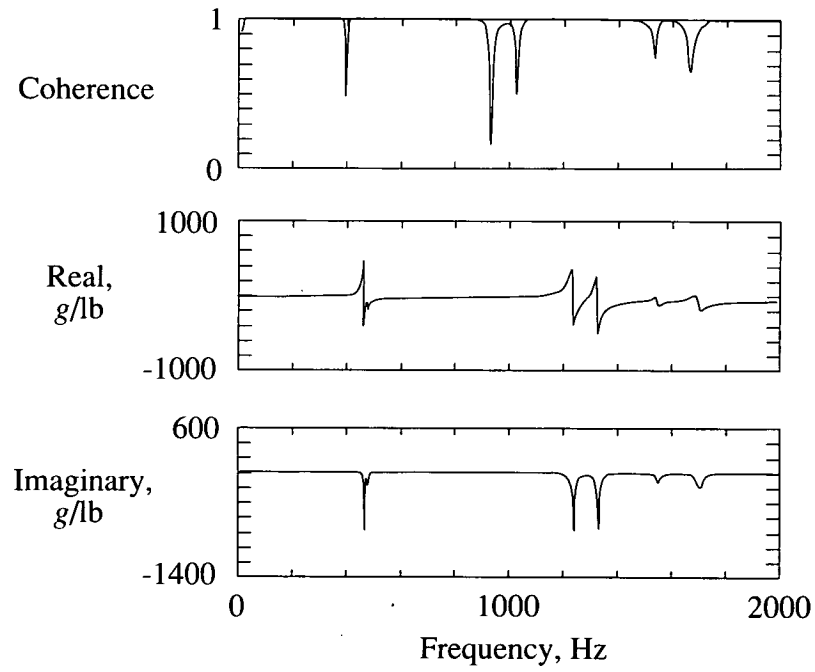


Figure 25.  $1Z_-$  driving point measurement for VS2.

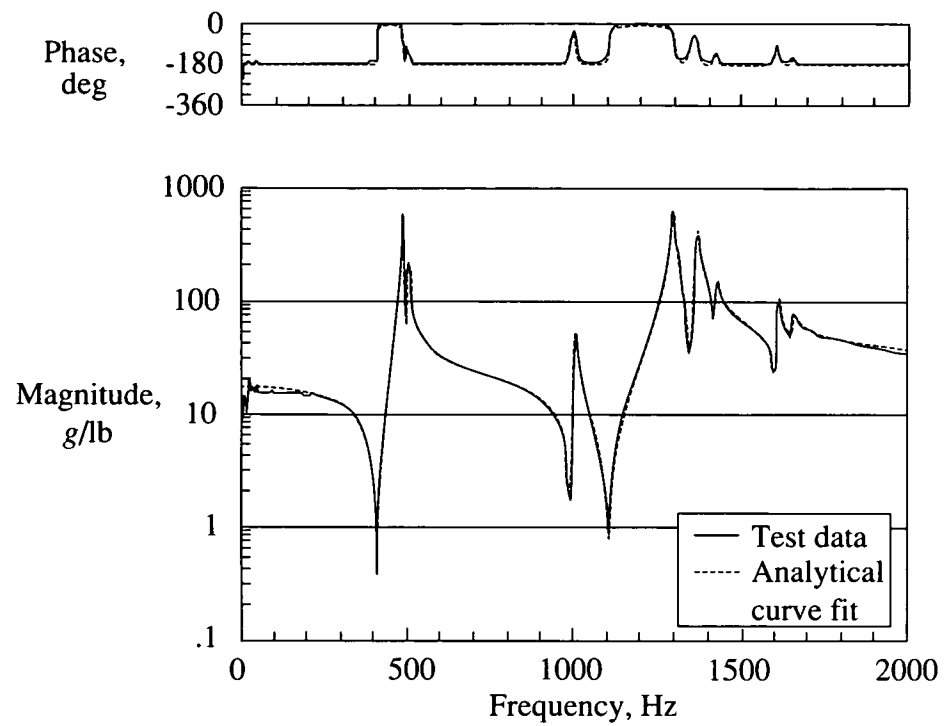


Figure 26. Frequency response function for VS3.

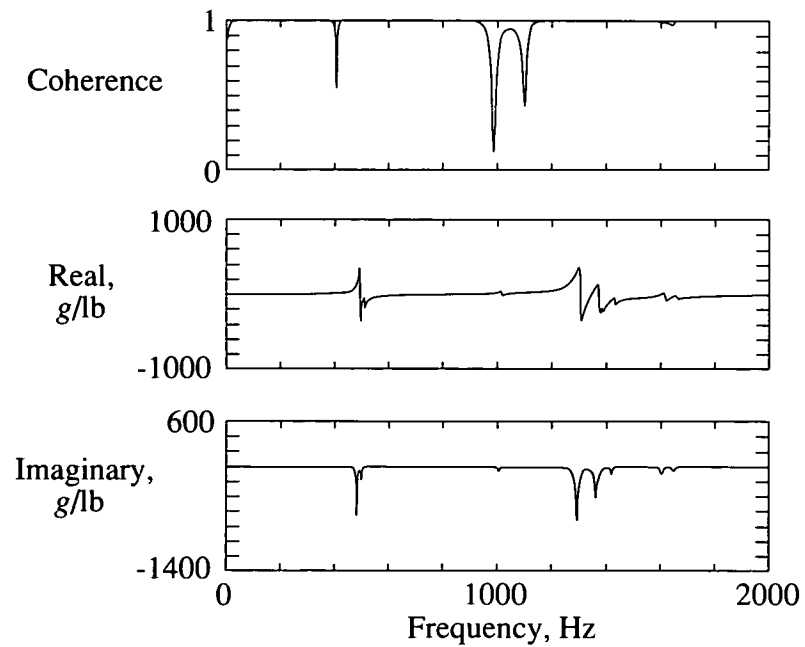


Figure 27.  $1Z_-$  driving point measurement for VS3.

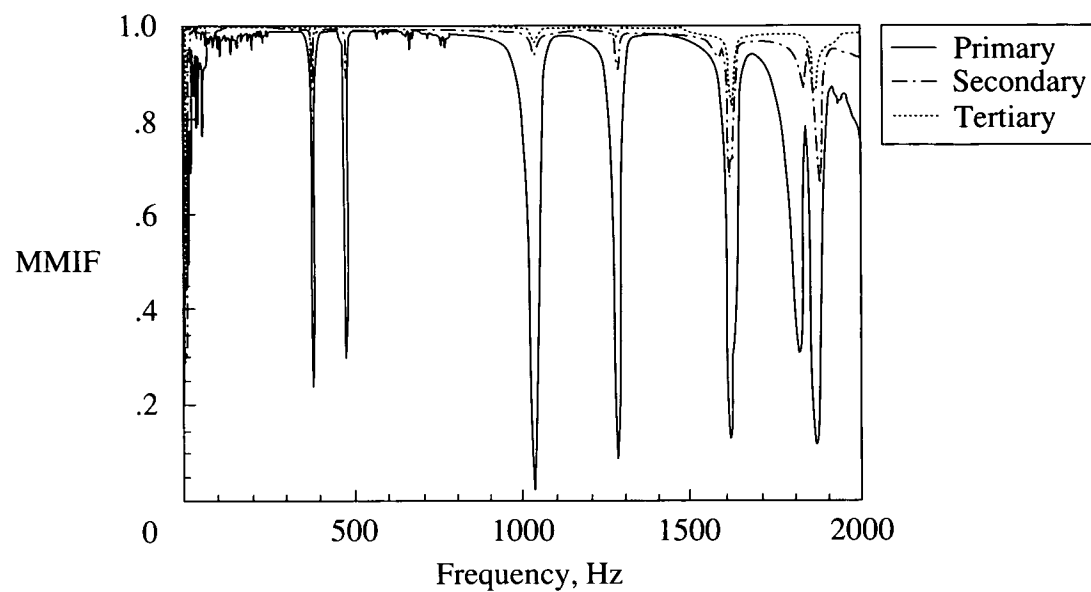


Figure 28. Multivariate mode indicator function for VE1.

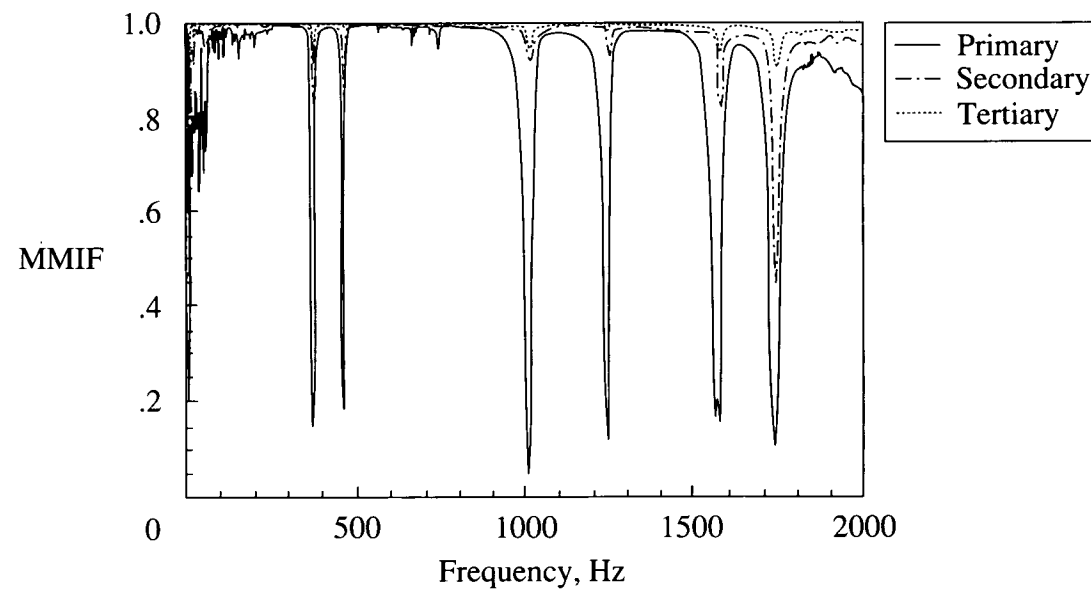


Figure 29. Multivariate mode indicator function for VE2.

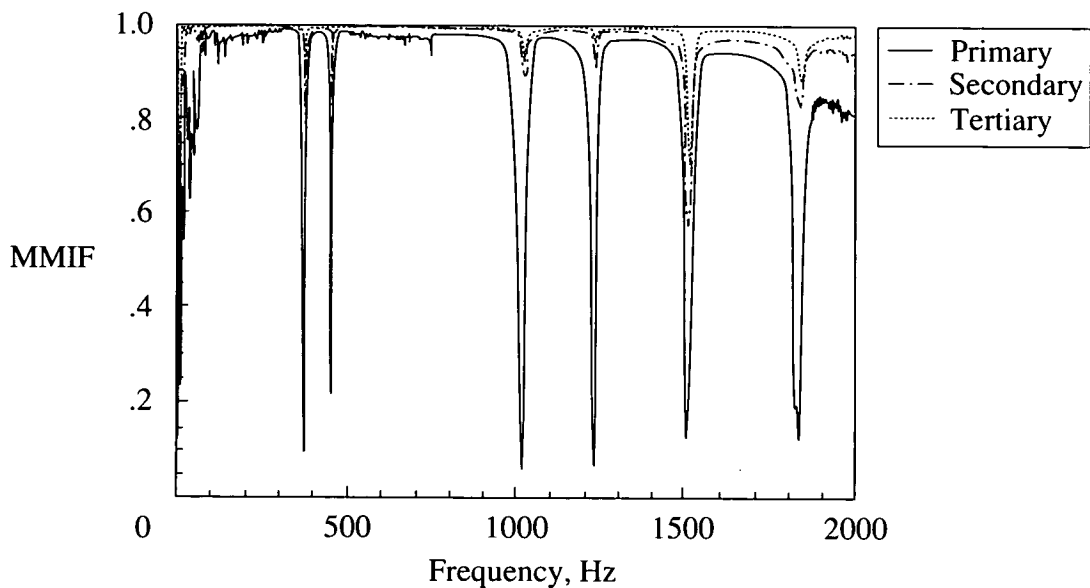


Figure 30. Multivariate mode indicator function for VE3.

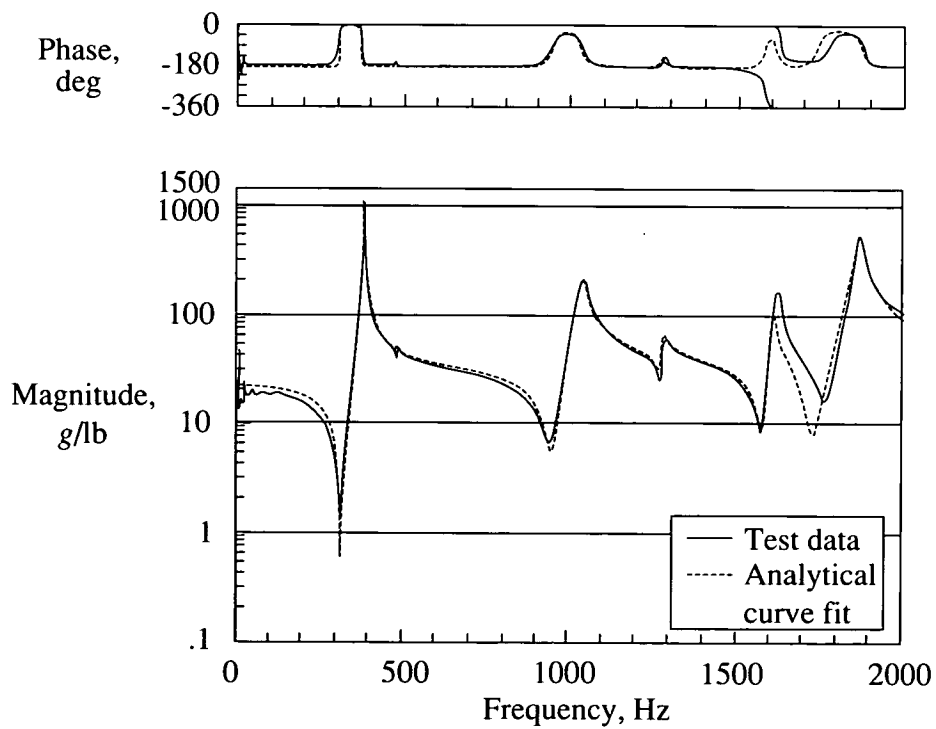


Figure 31. Frequency response function for VE1.

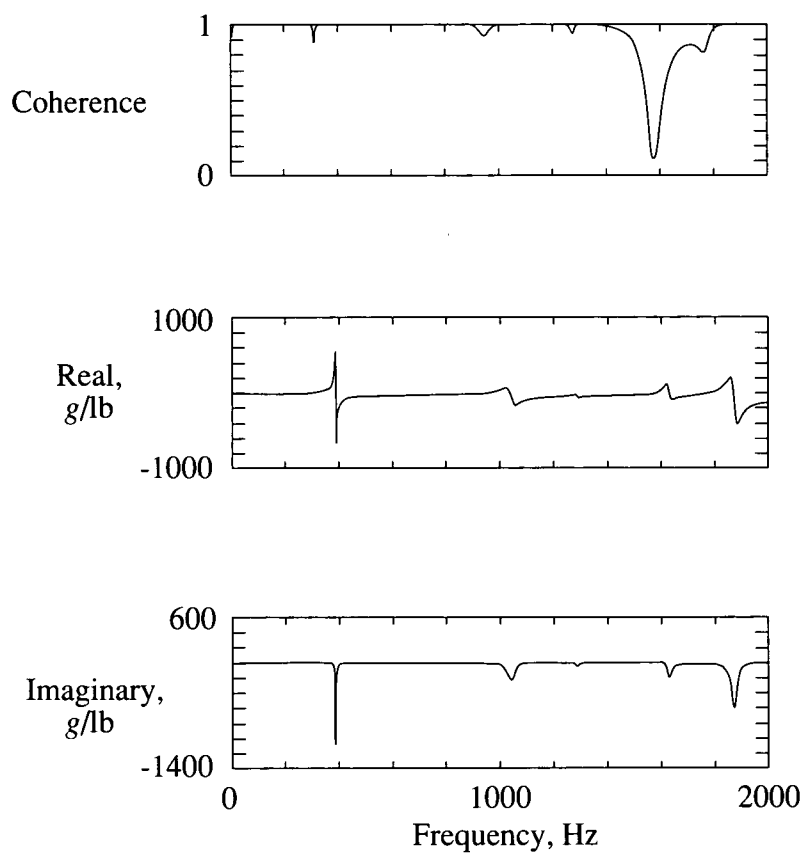
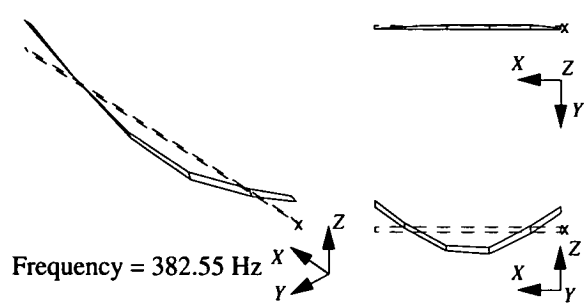
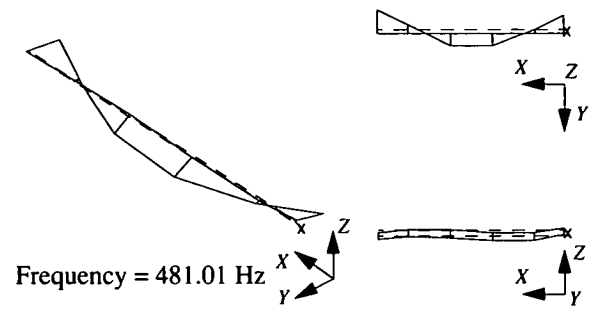


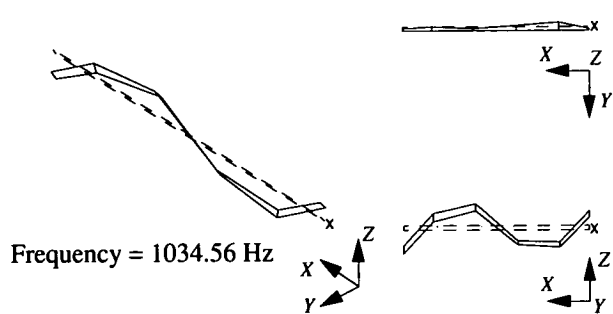
Figure 32.  $1Z_-$  driving point measurement for VE1.



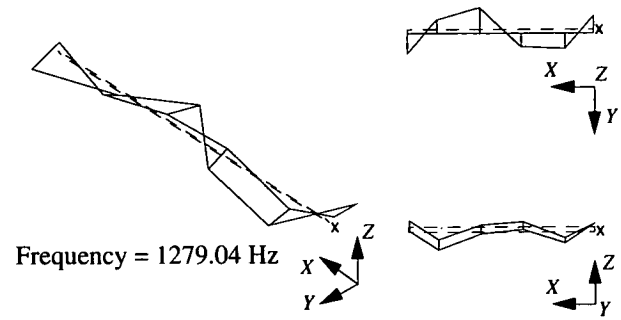
(a) First vertical bending.



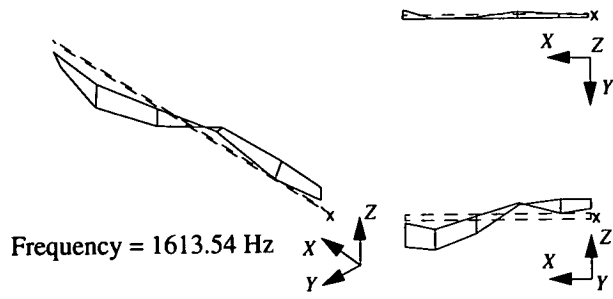
(b) First lateral bending.



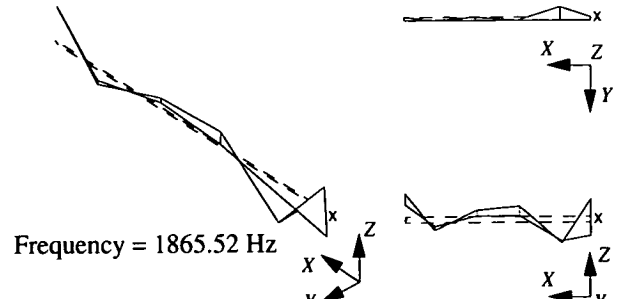
(c) Second vertical bending.



(d) Second lateral bending.



(e) First torsion.



(f) Third vertical bending.

Figure 33. Global mode shapes for VE1.

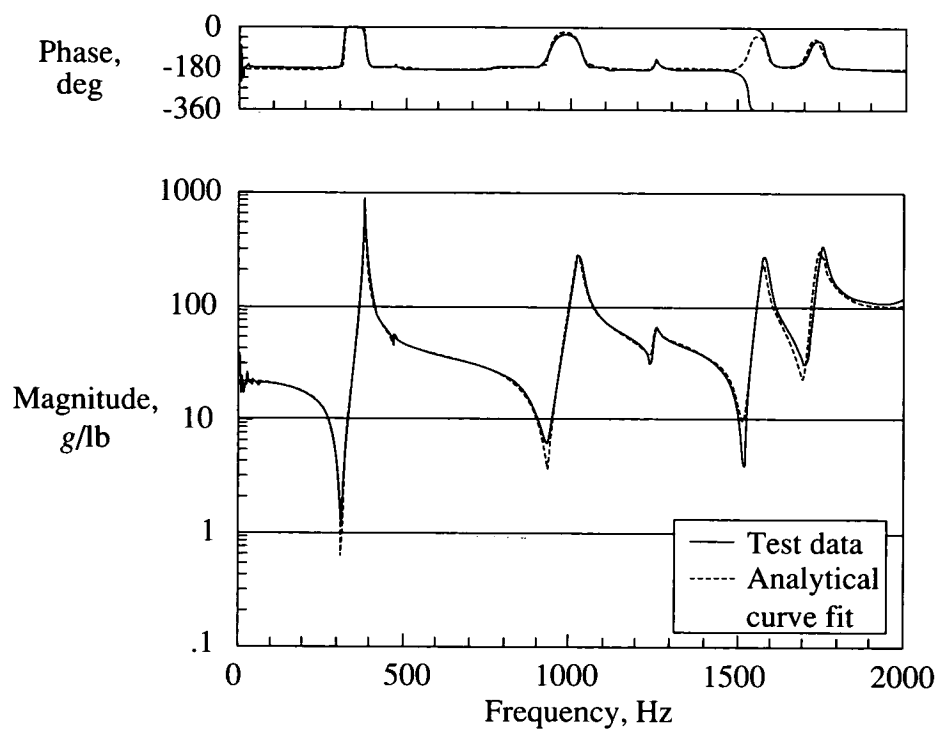


Figure 34. Frequency response function for VE2.

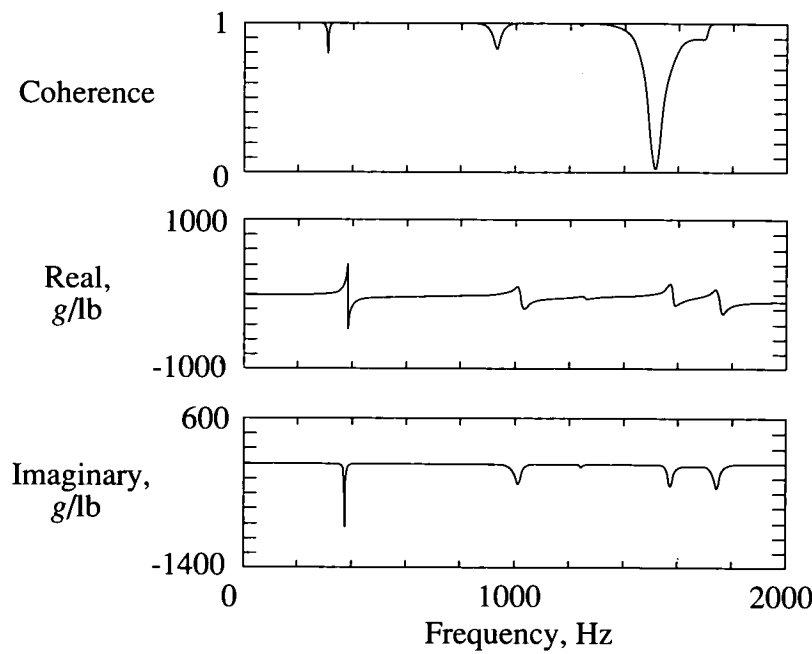


Figure 35.  $1Z_-$  driving point measurement for VE2.

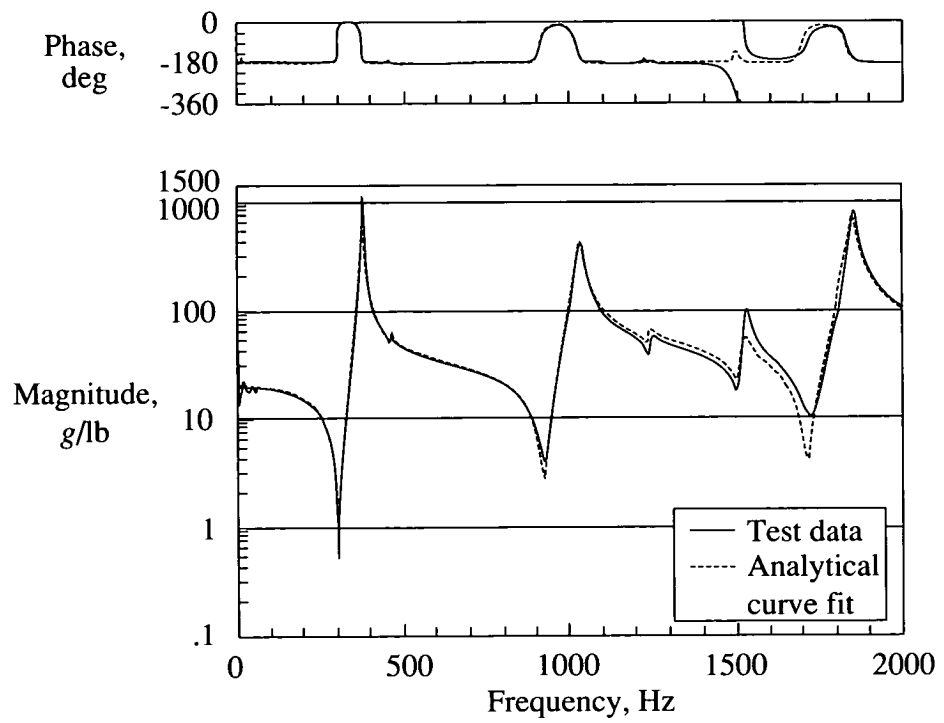


Figure 36. Frequency response function for VE3.

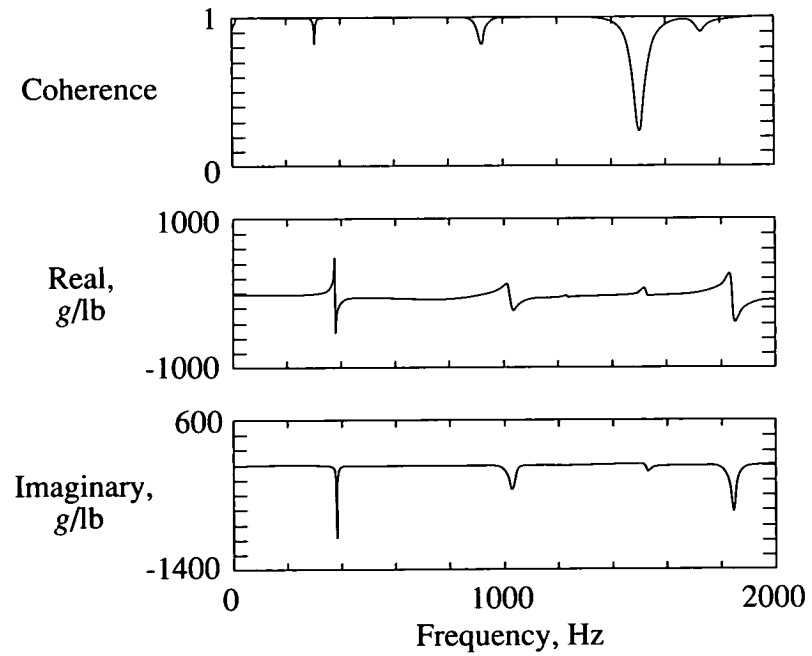


Figure 37.  $1Z_-$  driving point measurement for VE3.

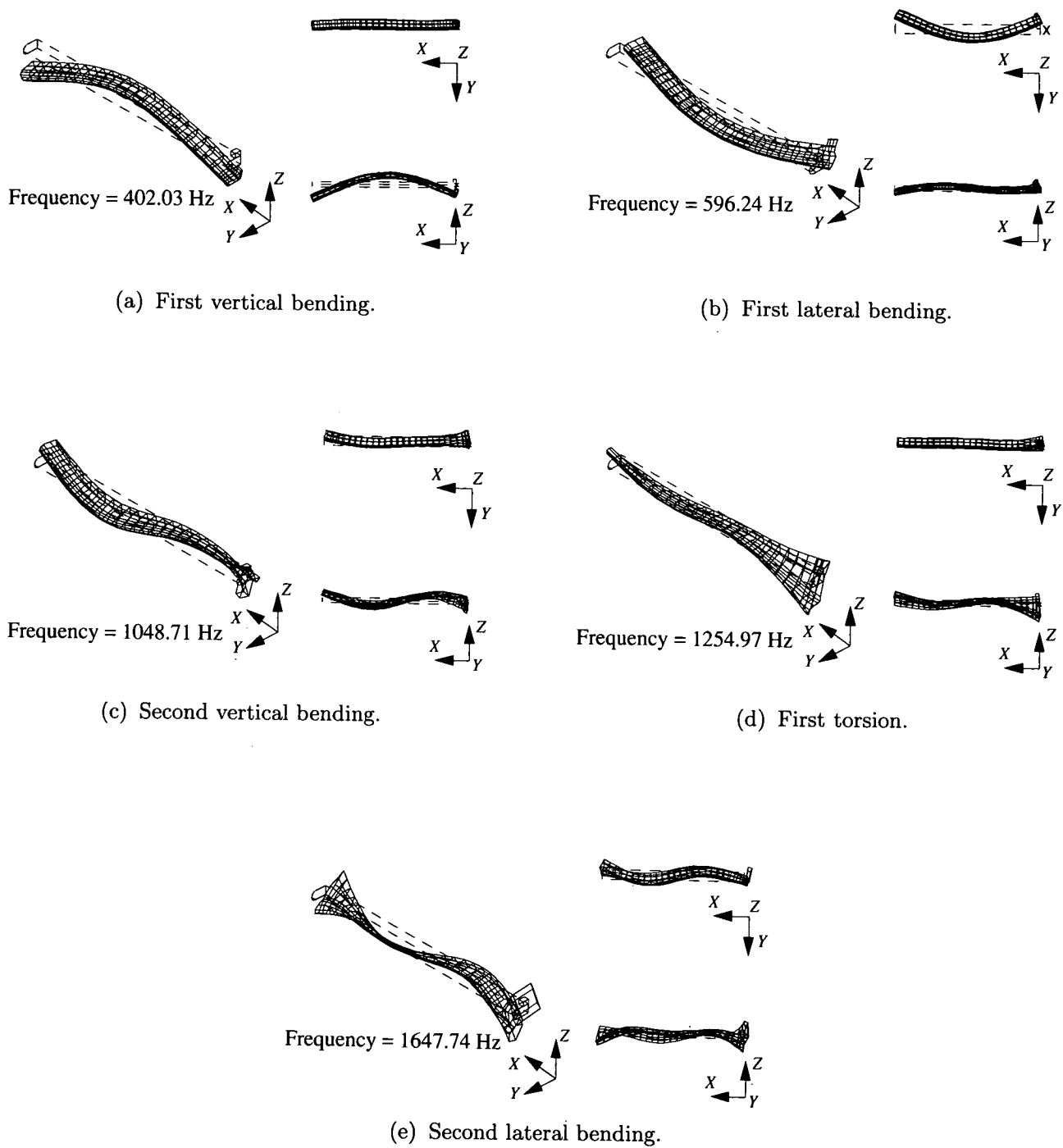
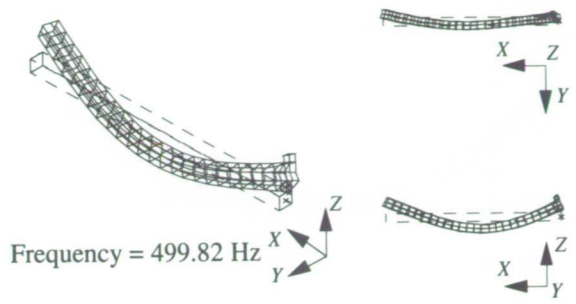
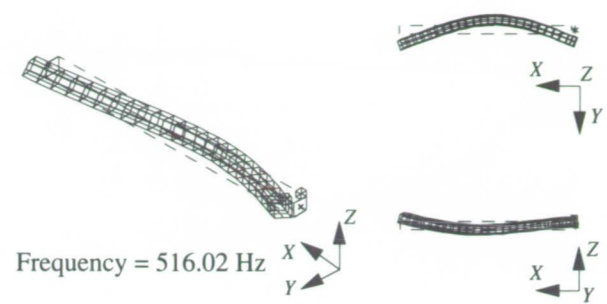


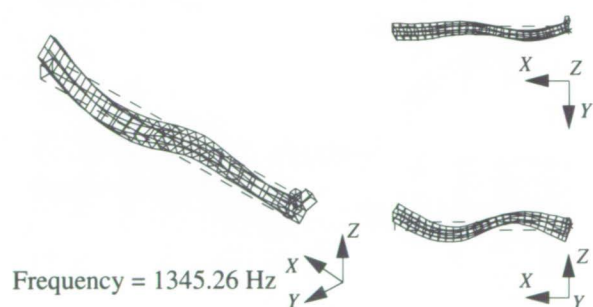
Figure 38. Global analytical mode shapes for VD1.



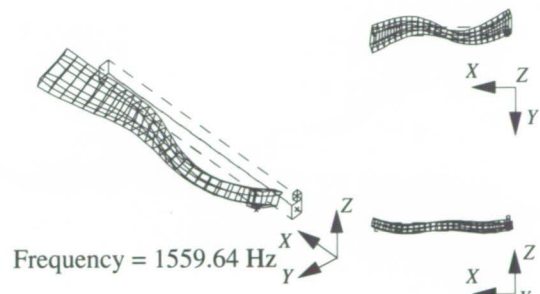
(a) First vertical bending.



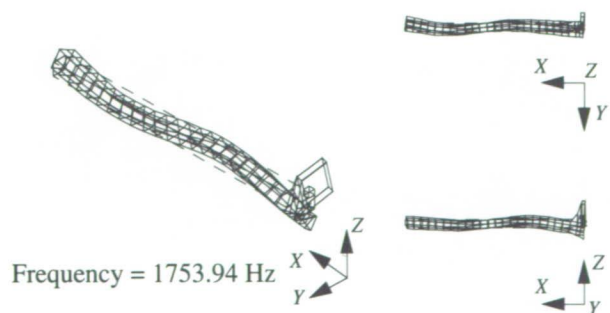
(b) First lateral bending.



(c) Second vertical bending.



(d) Second lateral bending.



(e) First torsion.

Figure 39. Global analytical mode shapes for VS1.

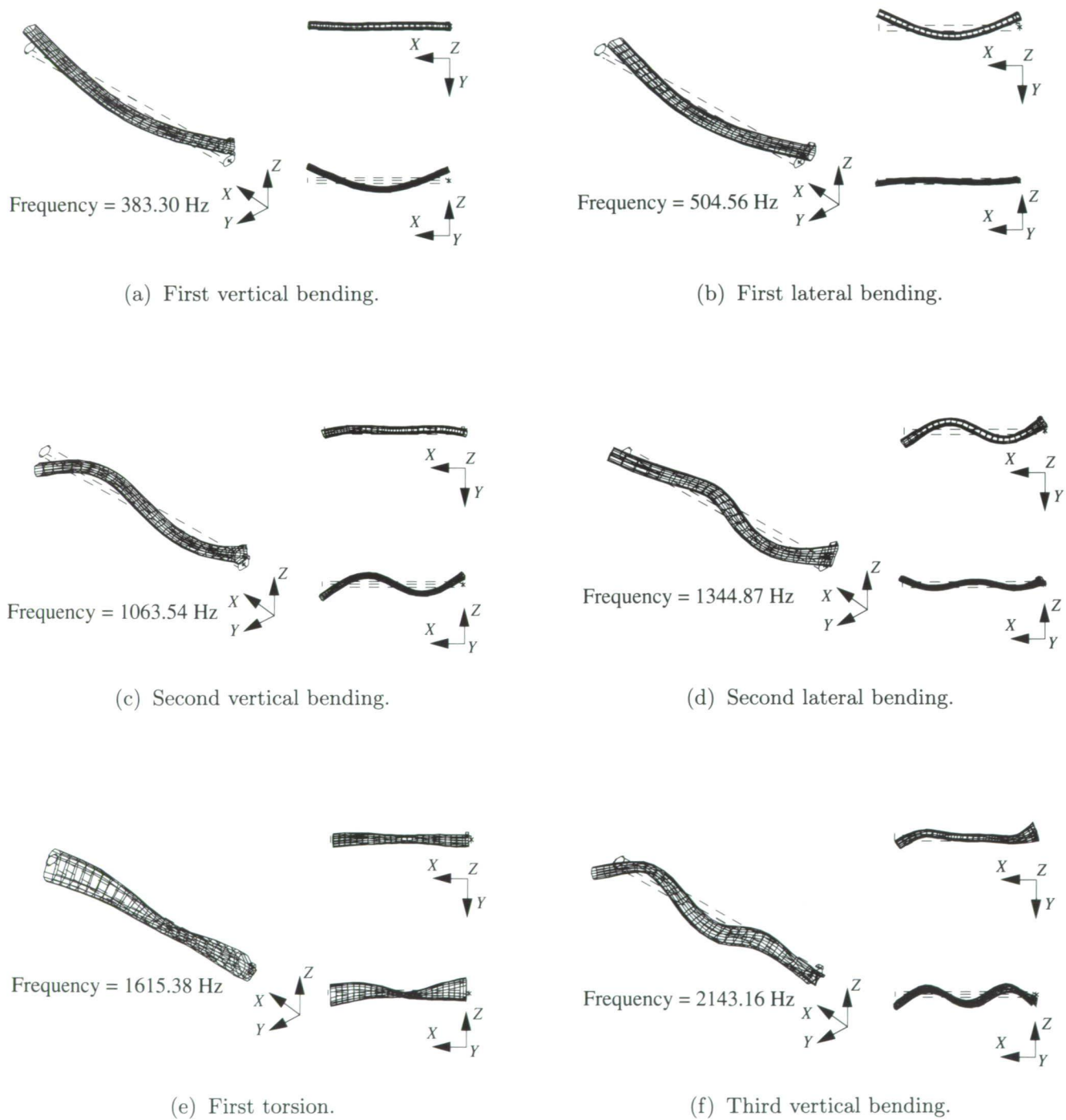


Figure 40. Global analytical mode shapes for VE1.

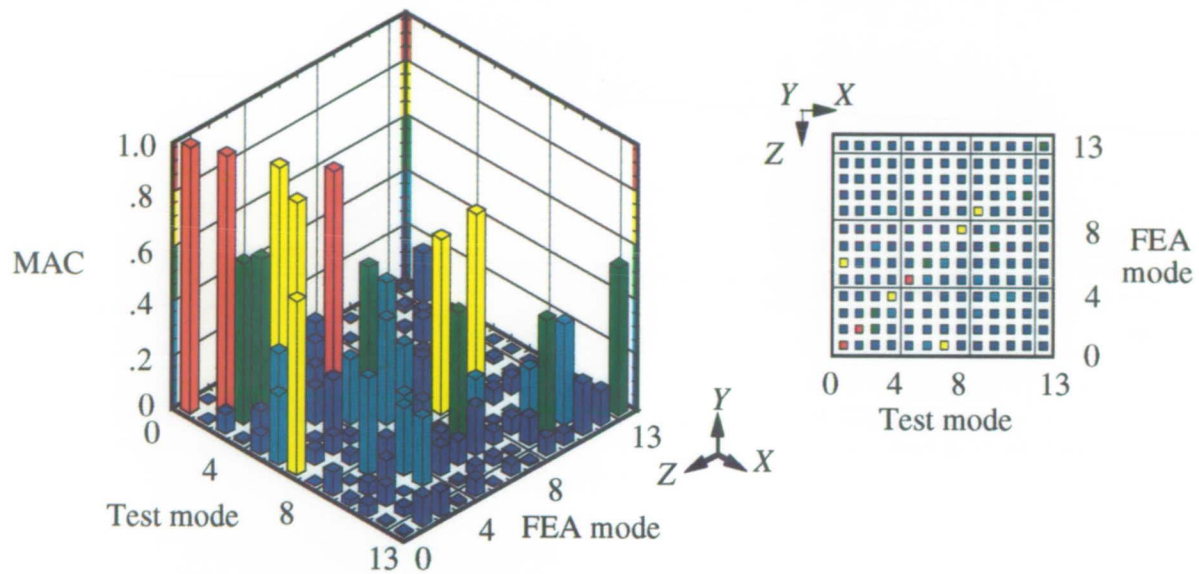


Figure 41. Modal assurance criteria matrix for VD1.

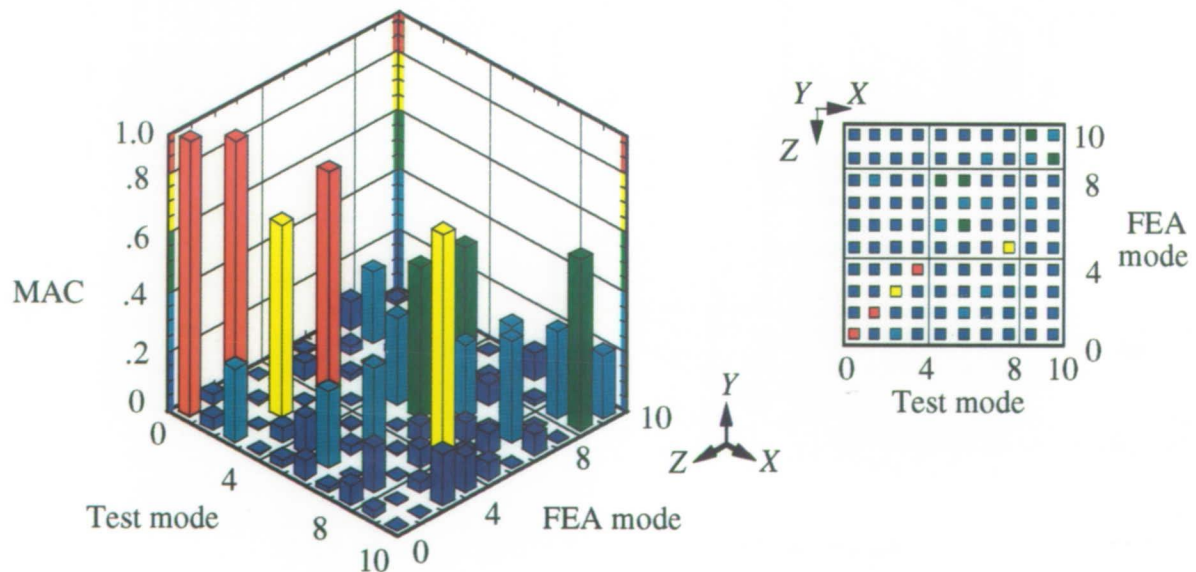
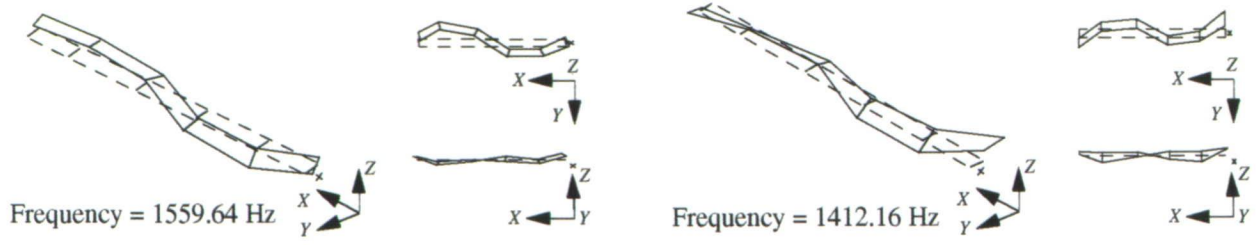


Figure 42. Modal assurance criteria matrix for VS1.



(a) Cross-mapped VS1 finite-element model.

(b) VS1 test model.

Figure 43. Test-analysis second lateral bending mode shapes for VS1.

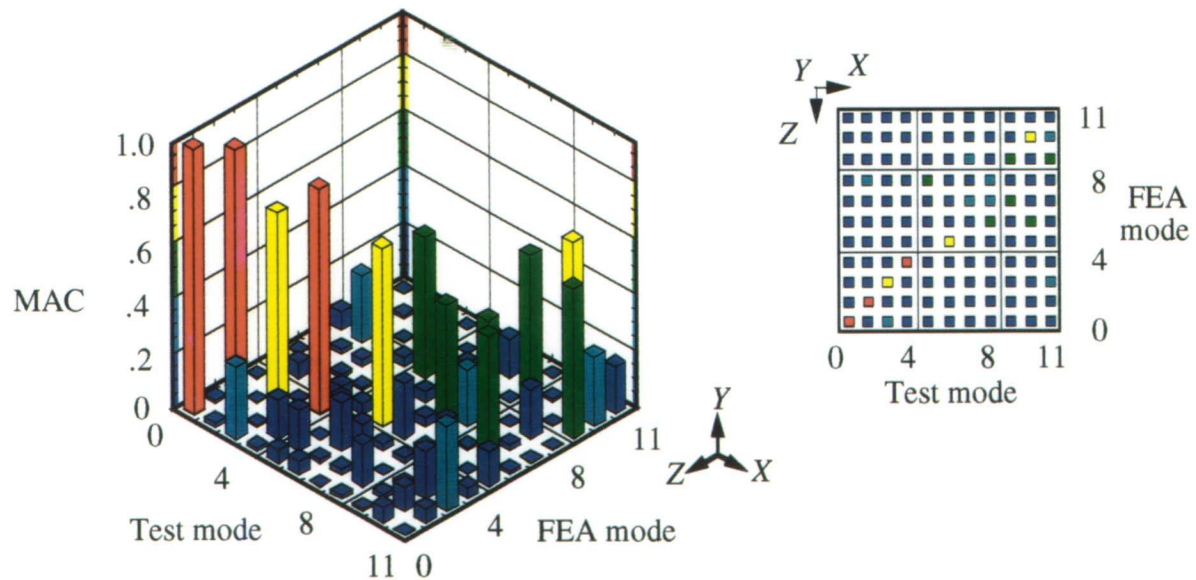


Figure 44. Modal assurance criteria matrix for VS2.

ORIGINAL PAGE  
COLOR PHOTOGRAPH

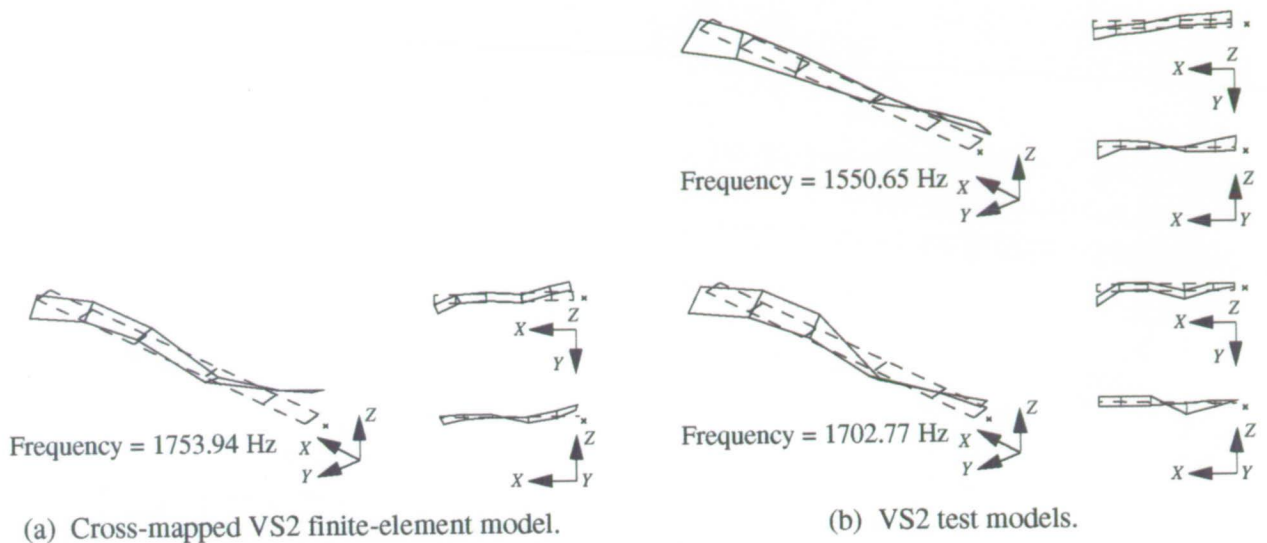


Figure 45. Test-analysis torsion mode shapes for VS2.

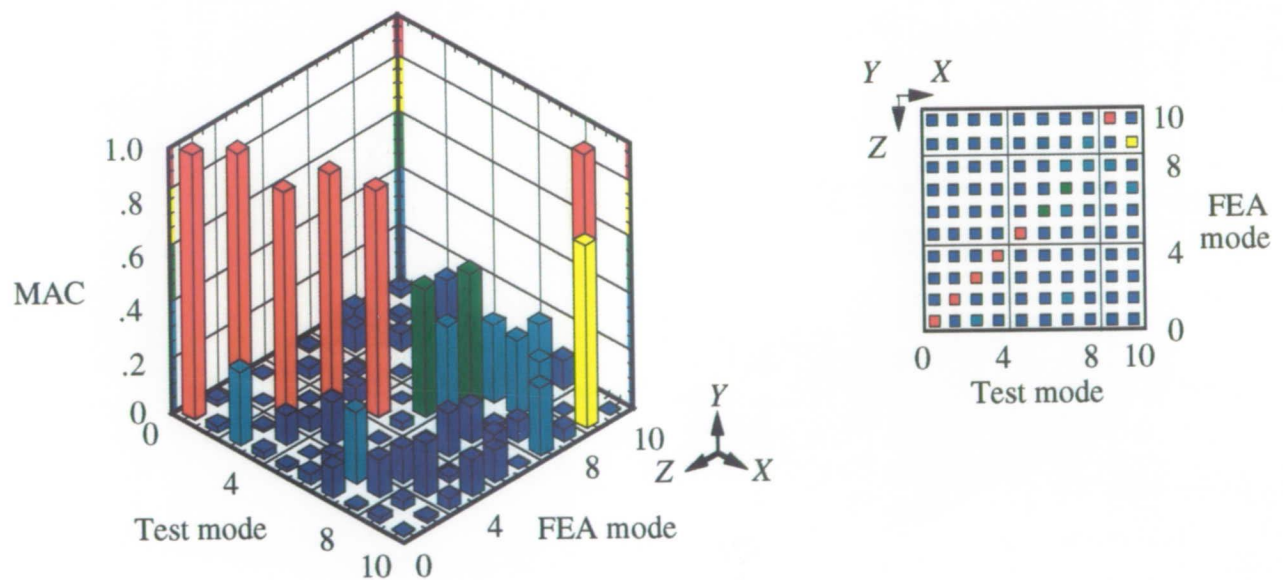


Figure 46. Modal assurance criteria matrix for VS3.

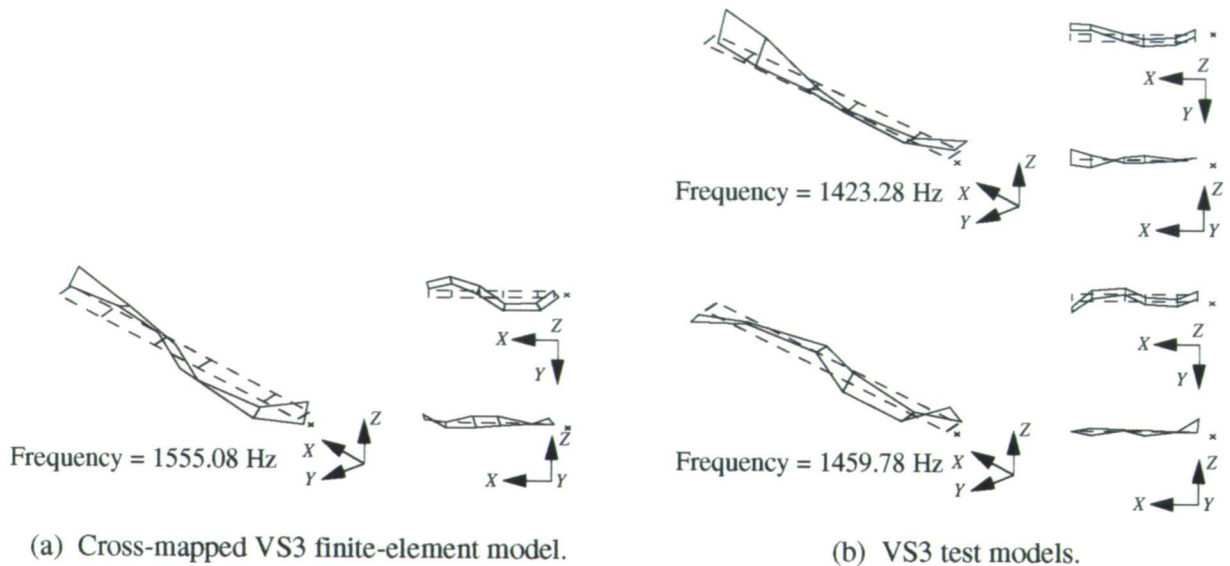


Figure 47. Test-analysis second lateral bending mode shapes for VS3.

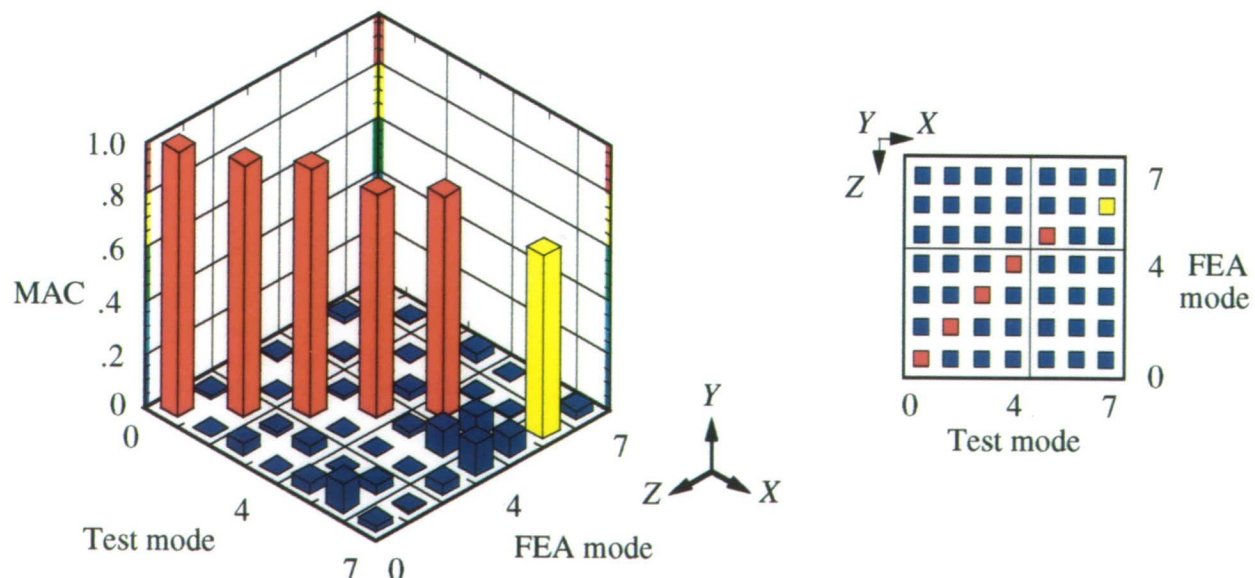


Figure 48. Modal assurance criteria matrix for VE1.

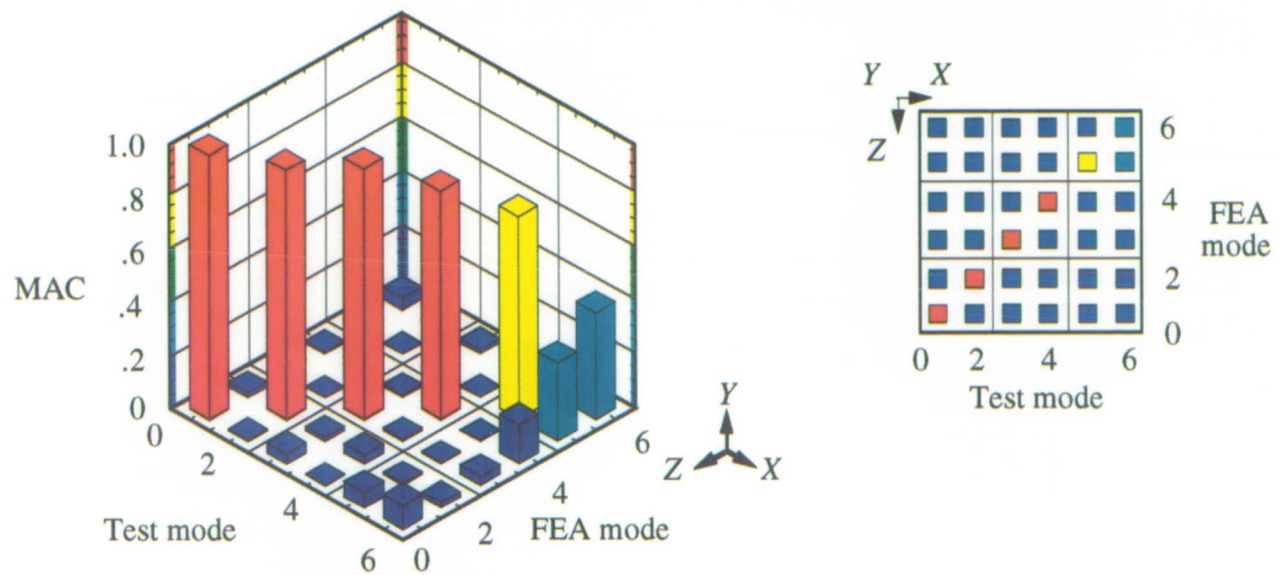


Figure 49. Modal assurance criteria matrix for VE2.

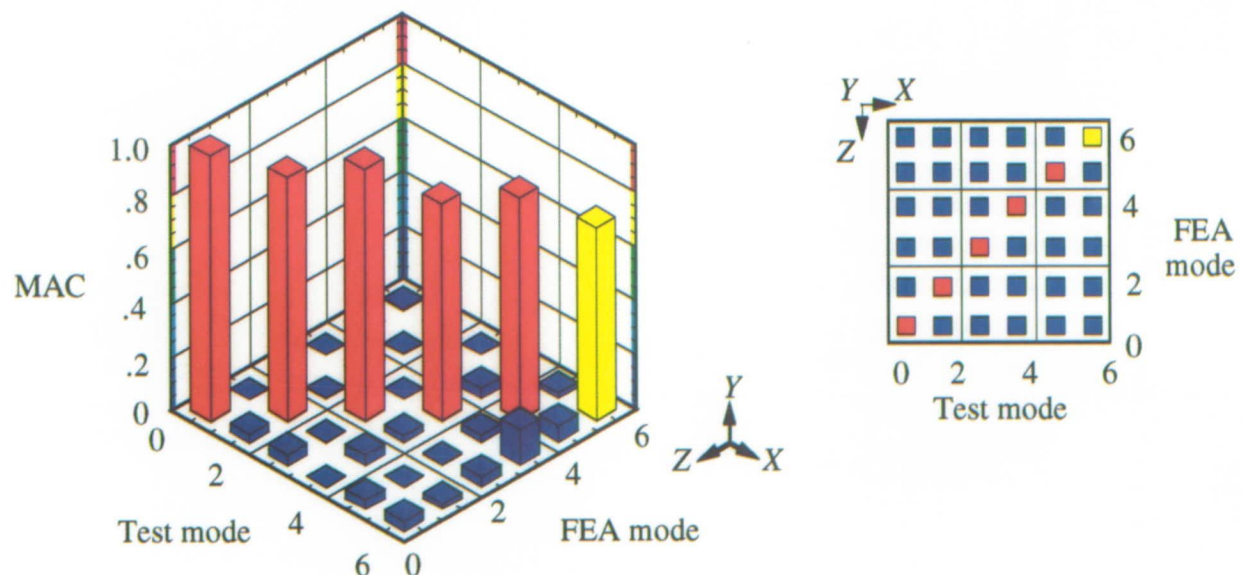


Figure 50. Modal assurance criteria matrix for VE3.

REPORT DOCUMENTATION PAGE			Form Approved OMB No. 0704-0188
<p>Public reporting burden for this collection of information is estimated to average 1 hour per response, including the time for reviewing instructions, searching existing data sources, gathering and maintaining the data needed, and completing and reviewing the collection of information. Send comments regarding this burden estimate or any other aspect of this collection of information, including suggestions for reducing this burden, to Washington Headquarters Services, Directorate for Information Operations and Reports, 1215 Jefferson Davis Highway, Suite 1204, Arlington, VA 22202-4302, and to the Office of Management and Budget, Paperwork Reduction Project (0704-0188), Washington, DC 20503.</p>			
1. AGENCY USE ONLY(Leave blank)	2. REPORT DATE	3. REPORT TYPE AND DATES COVERED	
	February 1993	Technical Paper	
4. TITLE AND SUBTITLE	Experimental and Analytical Investigation of Dynamic Characteristics of Extension-Twist-Coupled Composite Tubular Spars		5. FUNDING NUMBERS
6. AUTHOR(S)	Renee C. Lake, Amir P. Izadpanah, and Robert M. Baucom		PR 1L162211A47AB WU 505-63-36-01
7. PERFORMING ORGANIZATION NAME(S) AND ADDRESS(ES)	Vehicle Structures Directorate U.S. Army Research Laboratory Langley Research Center Hampton, VA 23681-0001		8. PERFORMING ORGANIZATION REPORT NUMBER
9. SPONSORING/MONITORING AGENCY NAME(S) AND ADDRESS(ES)	National Aeronautics and Space Administration Washington, DC 20546-0001 and U.S. Army Research Laboratory Adelphi, MD 20783-1145		10. SPONSORING/MONITORING AGENCY REPORT NUMBER
11. SUPPLEMENTARY NOTES	Lake: Vehicle Structures Directorate, U.S. Army Research Laboratory, Hampton, VA; Izadpanah: Sterling Software, Federal Systems Group, Palo Alto, CA; Baucom: Langley Research Center, Hampton, VA.		
12a. DISTRIBUTION/AVAILABILITY STATEMENT	Unclassified—Unlimited  Subject Category 39		12b. DISTRIBUTION CODE
13. ABSTRACT (Maximum 200 words)	The results from a study aimed at improving the dynamic and aerodynamic characteristics of composite rotor blades through the use of extension-twist coupling are presented. A set of extension-twist-coupled composite spars was manufactured with four plies of graphite-epoxy cloth prepreg. These spars were noncircular in cross-section design and were therefore subject to warping deformations. Three different cross-sectional geometries were developed: D-shape, square, and flattened ellipse. Three spars of each type were fabricated to assess the degree of repeatability in the manufacturing process of extension-twist-coupled structures. Results from free-free vibration tests of the spars were compared with results from normal modes and frequency analyses of companion shell-finite-element models. Five global modes were identified within the frequency range from 0 to 2000 Hz for each spar. The experimental results for only one D-shape spar could be determined, however, and agreed within 13.8 percent of the analytical results. Frequencies corresponding to the five global modes for the three square spars agreed within 9.5, 11.6, and 8.5 percent of the respective analytical results and for the three elliptical spars agreed within 4.9, 7.7, and 9.6 percent of the respective analytical results.		
14. SUBJECT TERMS	Anisotropy; Composite materials; Dynamic structural analysis; Elastic tailoring; Extension-twist coupling; Finite-element analysis		15. NUMBER OF PAGES
			56
17. SECURITY CLASSIFICATION OF REPORT	18. SECURITY CLASSIFICATION OF THIS PAGE	19. SECURITY CLASSIFICATION OF ABSTRACT	20. LIMITATION OF ABSTRACT
Unclassified	Unclassified		

National Aeronautics and  
Space Administration  
Code JTT  
Washington, D.C.  
20546-0001

Official Business

Penalty for Private Use, \$300

BULK RATE  
POSTAGE & FEES PAID  
NASA  
Permit No. G-27



POSTMASTER: If Undeliverable (Section 158  
Postal Manual) Do Not Return

---